A continuum mechanical surrogate model for atomic beam structures

Marcus G. Schmidt*[1], Ahmed E. Ismail†[1,2], and Roger A. Sauer‡[1]

[1]AICES Graduate School, RWTH Aachen University, Aachen, Germany
[2]Aachener Verfahrenstechnik: Molecular Simulations and Transformations, Faculty of Mechanical Engineering, RWTH Aachen University, Aachen, Germany

This is an author-created, un-copyedited version of an article accepted for publication in the *International Journal for Multiscale Computational Engineering*. Begell House Inc. is not responsible for any errors or omissions in this version of the manuscript or any version derived from it.

doi:10.1615/IntJMultCompEng.2015013568.

Starting from a fully atomistic system, we outline a general approach to obtain an approximate continuum surrogate model incorporating specific kinematic state variables. The continuum mechanical system is furnished with a hyperelastic material model. We then adapt the procedure to slender structures with beam-like character, such as Silicon nanowires or carbon nanotubes. The surrogate model can be described as a geometrically exact beam, which can be treated numerically using finite elements. Based on molecular dynamics simulations, we show how to obtain for a given atomistic beam system both a set of suitable deformed states as well as generalized stress and strain measures. Finally, we benchmark the obtained continuum model by assessing its accuracy for a beam coming into contact with an infinite Lennard-Jones wall.

1 Introduction

Recently, the mechanical behavior of nanoscale beam-like structures, whose extent in one spatial dimension is much larger than in the other two dimensions, has

*schmidt@aices.rwth-aachen.de
†aei@alum.mit.edu
‡sauer@aices.rwth-aachen.de

attracted much interest. Examples of beam-like structures include nanowires (also known as nanorods or nanobeams), which are very small metal or semiconductor crystalline structures used to create field-effect transistors, LEDs, nanoscale lasers, and many other devices. They also form a promising class of candidates for use in nano-electromechanical systems (NEMS) [1]. Another example are carbon nanotubes (CNT), which can be thought of as rolled-up graphene sheets and are of interest due to their remarkable mechanical properties, such as very high tensile strength and Young's modulus [2], as well as their tunable electrical behavior [3]. Further examples include cellulose bundles [4]; biopolymers [5–7], including DNA [8]; and other organic macromolecules.

In this work, we develop a method to systematically obtain a hyperelastic material description from a molecular dynamics (MD) model of an atomistic beam-like system. No special assumptions are made in advance about the interatomic potential governing the material. The resulting information can then be used as an efficient continuum mechanical surrogate model for quasi-static simulations, which, in contrast to existing models, represents the system at a finite temperature. This continuum model is based on geometrically exact beams, also known as the special Cosserat theory of rods) [9, 10], and consists of a homogenized description of the material behavior of the original structure as well as of its geometrical and mass-related properties. The numerical treatment is handled by a suitable finite element method (FEM). Subsequent applications then require only problem-specific data such as applied forces or moments and interaction energies with external bodies. We also show how the required steps fit into an abstract procedure that can be adapted to other continuum theories that incorporate different kinematic assumptions and state variables.

General methods to identify constitutive laws for beam structures and related continuum mechanical systems, such as shells or sheets, have already received considerable attention. Originally formulated for bulk systems, the Cauchy-Born rule (CBR), see for example [11], relates macroscopic deformations (usually given as deformation gradients) to microscopic ones but is by itself valid only at zero temperature. The interatomic potential is then evaluated for these displaced atomic positions. Several variants of the bulk CBR have been suggested. For example, Arroyo and Belytschko [12] develop an exponential CBR to study the mechanical behavior of carbon nanotubes. A further extension is the local CBR [13], which provides a framework to obtain atomistically derived constitutive laws for a large class of continuum theories based on various kinematic constraints. Another version of the CBR is employed in the objective quasicontinuum (OQC) method [14], which represents an atomic system exhibiting an inherent repeat pattern, so-called fundamental domains, through an array of a few elements underlaid with copies of the fundamental domain. The authors then demonstrate the feasibility of this

approach for a copper nanobeam. Friesecke and James [15] and Schmidt [16] have developed a theoretical framework for constructing the (potential) energy of crystalline films and nanotubes. Chandraseker et al. [17] and Fang et al. [18] present an extended Cosserat beam theory that can undergo cross section deformations and describe the fitting of the potential energy based on quantum-mechanical calculations. Chen and Lee [19, 20] present a connection of micromorphic theory to MD.

The potential energy minimized in the zero-temperature case is much more accessible than the Helmholtz free energy, which is needed to derive stresses at isothermal thermodynamic equilibrium. The CBR allows the connection between macroscopic and microscopic strains to be expressed directly. Such relationships do not exist for finite temperatures and thus stresses can no longer be evaluated on the fly. Instead, one can approximate the free energy and its derivatives using methods such as the quasi-harmonic approximation [21] or the local harmonic approximation [22]. Alternatively, one can first determine the stress-strain relationship and then use a correspondingly fitted material law [23–25]. Here, we will follow this sequential approach as well. An alternative information-passing strategy is provided by the generalized mathematical homogenization (GMH) theory [26], in which the atomistic equations of motion are related to a coarse-scale description through suitably transformed coordinates. An asymptotic expansion of these equations then leads to a continuum description of the coarse scale that can be solved using a FEM. GMH has also been extended to finite temperatures [27] and successfully applied to heat conduction problems. The approach in the present work yields a parameterized constitutive law that can readily be used in existing finite-element codes. No restriction is imposed on the type of interatomic potentials; only Coulombic interactions typically are not captured, because of their long-range influence. The issue of capturing heat transfer behavior from atomistic simulations is further studied in Admal and Tadmor [28] and Davydov and Steinmann [29].

The remainder of this article is organized as follows. In section 2, we describe an abstract workflow for obtaining constitutive laws for continuum theories with arbitrary kinematics, which we illustrate for geometrically exact beams in section 3. Section 4 provides numerical results obtained for CNTs and silicon nanowires (SiNW). In particular, contact between these beam structures and Lennard-Jones walls is studied and explicit formulas for the interaction energy of undistorted beam cross sections with such walls are presented. Finally, conclusions and an outlook are provided in section 5.

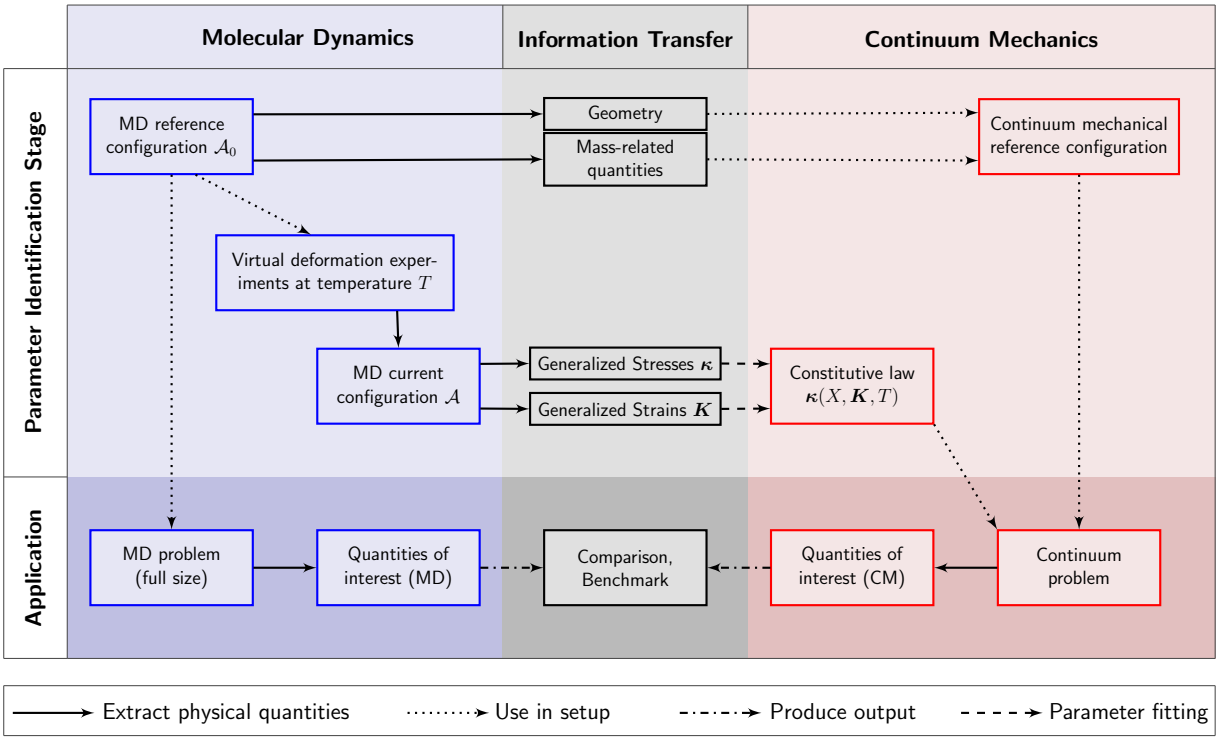

Figure 1: The key steps for obtaining and validating a temperature-specific hyperelastic material law for a continuum system.

2 Outline of a general procedure

Before exploring how to transfer an atomistic beam model to a continuous surrogate model, we introduce the general workflow, shown in figure 1, which is valid for different kinds of systems and continuum theories. The procedure is strictly sequential, with no flow of information from the continuum back to the atomistic side (which would represent a concurrent method). Our starting point is an atomistic, possibly coarse-grained, system consisting of N particles with positions $\boldsymbol{q} = (\boldsymbol{q}_1, \dots, \boldsymbol{q}_N)$ and linear momenta $\boldsymbol{p} = (\boldsymbol{p}_1, \dots, \boldsymbol{p}_N)$. Its instantaneous total energy is given by the Hamiltonian

$$H(\boldsymbol{q}, \boldsymbol{p}) = K(\boldsymbol{p}) + V_{\text{int}}(\boldsymbol{q}) + V_{\text{ext}}(\boldsymbol{q}), \tag{1}$$

where $K(\boldsymbol{p}) = \frac{1}{2}\sum_{i=1}^{N}(\boldsymbol{p}_i \cdot \boldsymbol{p}_i)/m_i$ denotes the kinetic energy in terms of the linear momenta $\boldsymbol{p}_i$ and V_{int} is the frame-indifferent part of the internal energy which accounts for interactions among the system's particles. V_{ext} subsumes additional interactions with the environment. Now consider that the system is at a (metastable) equilibrium that we take as the initial state. For solid-like materials, we can define an *atomistic reference configuration* [21], as the set of all time-averaged mean

positions in the initial state:

$$\mathcal{A}_0 = \left\{ \overline{\boldsymbol{Q}}_i \;\middle|\; i = 1, \ldots, N \right\}, \quad \overline{\boldsymbol{Q}}_i := \langle \boldsymbol{q}_i \rangle. \tag{2}$$

Now suppose that we represent the system using a still-undetermined continuum theory, in which each continuum point is underlaid with a local thermodynamic system having n kinematic state variables or generalized strains $\boldsymbol{K} = (K_1, \ldots, K_n)$. In three-dimensional continuum mechanics these would usually correspond to, for example, the $n = 6$ stretch components of the deformation gradient $\boldsymbol{F}$. These are also represented by the stretch tensor $\mathbf{U}$ of the polar decomposition $\boldsymbol{F} = \mathbf{RU}$. Frame-indifference implies the thermodynamic system is independent of the three rotatory components of $\mathbf{R}$.

Our goal is a continuum mechanical surrogate model for atomistic problems representing quasi-static processes at constant temperature and with a fixed number of particles. Thus, a new atomistic state is obtained by a series of small perturbations of the boundary conditions in an NVT ensemble and subsequent equilibrations, corresponding to applications where observation times are longer than equilibration times and in particular longer than the time needed for any viscous processes. This suggests that it is sufficient to consider the functional relationship $\psi = \psi(X, \boldsymbol{K}, T)$ between the kinematic state and the Helmholtz free energy per unit mass at (quasi-)equilibrium, and to assume that the associated thermodynamic tensions or generalized stresses are given by

$$\boldsymbol{\kappa}(X, \boldsymbol{K}, T) = \frac{\partial}{\partial \boldsymbol{K}} \psi(X, \boldsymbol{K}, T), \tag{3}$$

which could, for example, correspond to the first Piola-Kirchhoff stress (divided by reference mass density). The possibility of an explicit dependence of the constitutive relations on the position is indicated by X, which specifies a material point in the reference configuration for a suitable coordinate system. In the three-dimensional case, this corresponds to a material coordinate $\boldsymbol{X}$, in which case we use a bold face symbol. It is known from statistical mechanics that the absolute Helmholtz free energy of a system at equilibrium with a homogeneous kinematic state $\boldsymbol{K}$ is

$$\Psi = \Psi(\boldsymbol{K}, T) = -k_B T \ln Z(\boldsymbol{K}, T), \tag{4}$$

where the canonical partition function is given by

$$Z(\boldsymbol{K}, T) = \frac{1}{h^{3N} N_1! \cdots N_s!} \int_{\mathcal{P}(\boldsymbol{K})} \exp\left(- H(\boldsymbol{q}, \boldsymbol{p}) / k_B T \right) d\boldsymbol{q} d\boldsymbol{p} \tag{5}$$

with a total of $N = N_1 + \cdots + N_s$ particles of s different species [30]. The phase space $\mathcal{P}(\boldsymbol{K}) \in \mathbb{R}^{6N}$ containing elements $(\boldsymbol{q}, \boldsymbol{p})$ is chosen to contain the atomic

positions consistent with $\boldsymbol{K}$; usually no restrictions are placed on the momenta. This establishes the connection between the atomistic degrees of freedom and the macroscopic free energy. It is clear that the $6N$-fold integral in (5), as well as partial derivatives of Ψ or of the density ψ usually cannot be evaluated in closed form. Fortunately, these derivatives, such as stresses, can be approximated as time averages using MD.

The main task now is to determine the stress-strain relationship between $\boldsymbol{\kappa}$ and $\boldsymbol{K}$ in (3). We proceed as follows. Suppose that the atomic reference configuration $\mathcal{A}_0$ represents a *calibration system* used only to obtain the desired constitutive relation. $\mathcal{A}_0$ may be much smaller than the system sizes of the target applications, but is still large enough for adequate statistical sampling.

We define a set of *virtual deformation experiments* (VDE), a set of boundary conditions applied to $\mathcal{A}_0$ that drive the system to a deformed configuration $\mathcal{A}$. The boundary conditions are quite arbitrary and could consist of, for example, displacing a subset of boundary atoms to a prescribed location or exerting additional forces on all or parts of the atoms. To mimic an isothermal deformation process at this stage, the displacements or forces of the VDEs are first imposed slowly and are followed by sufficient additional equilibration time. Another requirement is that the boundary conditions are chosen so that they neither restrict nor deflect the particles' movement in some inner region of the calibration system. Thus, when we determine values for the generalized stresses $\boldsymbol{\kappa}$ from the atomistic system, all thermal vibrations are taken into account. For example, the virial expression for the Cauchy stress [31] requires averaging over the individual linear momenta associated with the currently deformed state.

Finally, if we can also obtain expressions for the strains $\boldsymbol{K}$ based on the atomistic trajectories, we can carry out a parameter-fitting procedure to obtain a functional relationship such as (3). The method for obtaining generalized stresses and strains from atomistic simulations must be developed for each continuum theory that we want to use, as shown in the following section for geometrically exact beams. Another scenario which fits into this abstract workflow is provided in Schmidt et al. [25], which analyzes a three-dimensional polymeric system for which the stress-strain relationship cannot be obtained using a classical representative volume element.

The remaining steps in the workflow are the transfer of the initial geometry of $\mathcal{A}_0$ to the continuum mechanical model and the determination of quantities related to the masses of the atoms, such as mass density or inertia tensors. We refer to the constitutive law, together with this information, as the surrogate model. Afterwards, we can apply the constructed model. To validate our procedure, we set up a benchmark problem in section 4.1 at both atomistic and continuum scales, and then compare several resulting quantities of interest extracted from each test

case. Problem details such as the applied loading conditions are independent of the model construction stage. We do not expect to observe exact agreement in these comparisons as homogenized continuum descriptions are obtained and atomistic details are irrecoverably lost. Nevertheless, an approximate descriptions of the material behavior of nanoscale beams is very useful for applications involving one or more such beam structures, which may be larger or made of varying materials. Also for coupled methods that concurrently handle atomistic and continuum domains, one may need a reliable material description for the latter.

3 A surrogate model for beam-like atomic structures

We now set up a continuum mechanical surrogate model for atomic beam-like structures using the workflow outlined in section 2. This procedure can be adapted to any simulation where ordinary bulk representative volume elements cannot be constructed. The latter usually require full three-dimensional periodicity, so that a macroscopic strain $\boldsymbol{F}$ can be directly applied to the atomistic system, and stresses can be averaged over the whole domain. To overcome this restriction, we use an indirect approach, relating simultaneously determined stresses and strains in a set of deformed states for a calibration system which is as small as possible but still large enough to exhibit representative behavior. However, in the case of beams, the cross section used must be the same as in the intended application problem, since the extracted material properties strongly depend on the beam cross section.

3.1 Geometrically exact beams

We briefly present the main aspects of geometrically exact beams, adapted from Antman [32], Simo [9], and [10]. A beam is a slender three-dimensional body with stress-free reference configuration $\mathcal{B}_0$ and deformed current configuration $\mathcal{B}$. The former is given as a line of centroids $\mathbf{R}(S)$, parameterized with respect to the arc length: $|\mathbf{R}'| \equiv 1$. Here, $S \in \mathcal{I} = [0, L]$, where L is the total arc length. At every position S there is a circular cross section[1] $\mathcal{C} = \{\boldsymbol{\zeta} \in \mathbb{R}^2 \,|\, \|\boldsymbol{\zeta}\| \leq R_{\text{cs}}\}$ of radius R_{cs}. The cross sections' orientation in space is described through the plane spanned by two orthonormal director vectors $\boldsymbol{D}_\alpha(S)$, $\alpha = 1, 2$, which can vary over $\mathcal{I}$. If we define the domain $\mathcal{P} = \mathcal{C} \times \mathcal{I}$, the reference configuration can be parameterized through the mapping

$$\boldsymbol{\Phi} : \mathcal{P} \to \mathcal{B}_0, \quad (\boldsymbol{\zeta}, S) = \left(\zeta^1, \zeta^2, S\right) \mapsto \mathbf{R}(S) + \zeta^\alpha \boldsymbol{D}_\alpha(S), \tag{6}$$

[1] In general, there are no special requirements for the shape of the cross sections, nor must cross sections be identical at each arc length.

Figure 2: Schematic of a geometrically exact beam. Two exemplary cross sections are shown, through which the central line $\mathbf{r}$ (black) passes. Also shown are the three director vectors $\boldsymbol{d}_1$ (cyan), $\boldsymbol{d}_2$ (white), $\boldsymbol{d}_3$ (red).

where Einstein summation is implied for Greek index $\alpha = 1, 2$. At time t, the central line and directors attain new values $\mathbf{r}(S,t)$ and $\boldsymbol{d}_\alpha(S,t)$, respectively, which form the parameterization for the current configuration:

$$\boldsymbol{\varphi} : \mathcal{P} \times [0,\infty) \to \mathcal{B}, \quad (\boldsymbol{\zeta}, S, t) \mapsto \mathbf{r}(S,t) + \zeta^\alpha \boldsymbol{d}_\alpha(S,t) \tag{7}$$

The current directors $\boldsymbol{d}_\alpha$ are still orthonormal and describe an undistorted, planar cross section. One can thus obtain complete orthonormal bases by defining $\boldsymbol{D}_3 := \boldsymbol{D}_1 \times \boldsymbol{D}_2$ and $\boldsymbol{d}_3 := \boldsymbol{d}_1 \times \boldsymbol{d}_2$. These can be arranged as second-order tensors indicating the change of the moving director bases,

$$\boldsymbol{\Lambda}_0(S) = \boldsymbol{D}_i(S) \otimes \boldsymbol{E}^i \tag{8}$$

$$\boldsymbol{\Lambda}(S,t) = \boldsymbol{d}_i(S,t) \otimes \boldsymbol{E}^i. \tag{9}$$

with summation over the Latin index $i = 1, 2, 3$. A schematic illustration of such a beam is shown in figure 2. The composition

$$\boldsymbol{\chi}(\cdot,t) = \boldsymbol{\varphi}(\cdot,t) \circ \boldsymbol{\Phi}^{-1} : \mathcal{B}_0 \to \mathcal{B} \tag{10}$$

is then the usual deformation mapping from three-dimensional continuum mechanics. Substituting it into the balance equations of linear and angular momentum yields the governing equations for the beam, which are now reduced to one spatial dimension:

$$\mathbf{n}'(S,t) + \widetilde{\mathbf{n}}(S,t) = M_0(S)\ddot{\mathbf{r}}(S,t) \tag{11a}$$

$$\mathbf{m}'(S,t) + \mathbf{r}'(S,t) \times \mathbf{n}(S,t) + \widetilde{\mathbf{m}}(S,t) = \dot{\boldsymbol{\pi}}(S,t), \tag{11b}$$

where $\mathbf{n}$ is the stress-resultant force, $\mathbf{m}$ is the stress-resultant moment acting on a cross section, $\widetilde{\mathbf{n}}$ and $\widetilde{\mathbf{m}}$ are distributed external forces and torques per unit length, and where primes and dots denote partial derivatives with respect to S and t,

respectively. Conservation of mass is also presumed. Furthermore, we introduce

$$\boldsymbol{\pi}(S,t) = \boldsymbol{i}_\rho(S,t)\boldsymbol{w}(S,t) \qquad \text{(angular momentum of cross section)} \tag{12}$$

$$\boldsymbol{i}_\rho(S,t) = M_2^{\alpha\beta}(S)[\delta_{\alpha\beta}\boldsymbol{I} - \boldsymbol{d}_\alpha(S,t)\otimes\boldsymbol{d}_\beta(S,t)] \qquad \text{(spatial inertia tensor)} \tag{13}$$

$$\boldsymbol{w}(S,t) = \operatorname{ax}\big(\dot{\boldsymbol{\Lambda}}(S,t)\boldsymbol{\Lambda}(S,t)^T\big) \qquad \text{(angular velocity vector)} \tag{14}$$

where $\operatorname{ax}(\cdot)$ returns the axial vector of a skew-symmetric second-order tensor. Finally we introduce the zeroth, first and second moments of mass of the cross section

$$M_0(S) = \int_{\mathcal{C}} \rho_0(\boldsymbol{\zeta},S)\,d\boldsymbol{\zeta}, \tag{15}$$

$$M_1^\alpha(S) = \int_{\mathcal{C}} \zeta^\alpha \rho_0(\boldsymbol{\zeta},S)\,d\boldsymbol{\zeta}, \tag{16}$$

$$M_2^{\alpha\beta}(S) = \int_{\mathcal{C}} \zeta^\alpha\zeta^\beta \rho_0(\boldsymbol{\zeta},S)\,d\boldsymbol{\zeta}, \tag{17}$$

for the reference mass density $\rho_0(\boldsymbol{\zeta},S)$. These can be interpreted as mass density, centroid and moment of inertia of the cross section, respectively. For simplicity, (11) already assumes that $M_1^\alpha \equiv 0$ for $\alpha = 1,2$. The unknowns are the central line $\mathbf{r}$ and the rotation $\boldsymbol{\Lambda}$. The stress-resultant force $\mathbf{n}$ and moment $\mathbf{m}$ act as generalized stresses, and are obtained as partial derivatives of the free energy. The kinematic descriptors are given by the following strain measures [33]:

$$\boldsymbol{\Gamma} = \boldsymbol{\Lambda}^T\mathbf{r}' - \boldsymbol{\Lambda}_0^T\mathbf{R}' \tag{18a}$$

$$\boldsymbol{\Omega} = \operatorname{ax}\big(\boldsymbol{\Lambda}^T\boldsymbol{\Lambda}' - \boldsymbol{\Lambda}_0^T\boldsymbol{\Lambda}_0'\big), \quad \widehat{\boldsymbol{\Omega}} = \boldsymbol{\Lambda}^T\boldsymbol{\Lambda}' - \boldsymbol{\Lambda}_0^T\boldsymbol{\Lambda}_0', \tag{18b}$$

where $\widehat{\cdot}$ gives the skew-symmetric tensor for a given axial vector. The first strain $\boldsymbol{\Gamma}$ captures shear and axial extension, while $\boldsymbol{\Omega}$ is associated with bending and twisting. Obviously, this formulation neglects possible changes in the cross-sectional shape, such as warping or ovalization, although extensions exist to account for these [34–39]. This typically leads to additional kinematic descriptors which must obey additional balance laws. However in the standard case as described above, the constitutive relations are given for the material counterparts $\mathbf{N}$, $\mathbf{M}$ of force and moment:

$$\mathbf{n} = \boldsymbol{\Lambda}\mathbf{N}, \quad \mathbf{N} = \partial_{\boldsymbol{\Gamma}}\psi(S,\boldsymbol{\Gamma},\boldsymbol{\Omega}) \tag{19a}$$

$$\mathbf{m} = \boldsymbol{\Lambda}\mathbf{M}, \quad \mathbf{M} = \partial_{\boldsymbol{\Omega}}\psi(S,\boldsymbol{\Gamma},\boldsymbol{\Omega}) \tag{19b}$$

Our main task is to determine the Helmholtz free energy (per unit reference length) ψ. Numerical treatments of the PDE system (11) have been thoroughly studied

[40–45]. One particular problem here is the proper representation and integration of the rotation, which must remain in $SO(3)$ and be adequately interpolated at the quadrature points [46]. The most frequently used approach is a quaternion-based formulation [40, 47–49]. We base our implementation on the work of Celledoni and Säfström [50].

3.2 Transfer of geometry and mass-related quantities

Given an atomistic reference configuration $\mathcal{A}_0$ of initial mean positions $\overline{\boldsymbol{Q}}_i$, the first task in parameterizing the continuum model is to determine the initial position of the line of centroids $\mathbf{R}(S)$ and the moving basis of directors $\boldsymbol{\Lambda}_0(S)$, $S \in \mathcal{I}$. We assume that the reference line of centroids is aligned along the z-axis, $\mathbf{R}(S) = S \cdot \boldsymbol{E}_3$, $S \in \mathcal{I}$, and that the directors have no initial rotation, $\boldsymbol{\Lambda}_0 \equiv \boldsymbol{I}$. We call this the *canonical* reference configuration shown in figure 6a. To approximately reconcile a set of given initial positions $\overline{\boldsymbol{Q}}_i$ with this assumption, we identify a rigid transformation

$$\mathcal{T}(\boldsymbol{X}) = \mathbf{S}\boldsymbol{X} + \boldsymbol{C}, \quad \mathbf{S} \in SO(3), \boldsymbol{C} \in \mathbb{R}^3, \tag{20}$$

that satisfies the following requirements when applied to the mean positions $\overline{\boldsymbol{Q}}_i$:

1. The z-axis is chosen to be the axis line of the slenderest cylinder containing all reference mean positions $\overline{\boldsymbol{Q}}_i$, so that the transformed reference configuration $\mathcal{T}(\mathcal{A}_0)$ lies along the z-axis. The beam's length L is then the difference of the largest and smallest z components.

2. The transformed cross section centroids should, on average, lie on the z-axis:

$$\langle M_1^\alpha \rangle_{\mathcal{I}} = \frac{1}{L} \int_{\mathcal{I}} M_1^\alpha(S)\, dS \stackrel{!}{=} 0, \quad \alpha = 1, 2 \tag{21}$$

3. The principal axes of inertia of the transformed cross sections should, on average, be aligned along the x- and y-axes:

$$\left\langle M_2^{12} \right\rangle_{\mathcal{I}} = \left\langle M_2^{21} \right\rangle_{\mathcal{I}} = \frac{1}{L} \int_{\mathcal{I}} M_2^{12}(S)\, dS \stackrel{!}{=} 0 \tag{22}$$

The calibration system is chosen large enough so that the average moments of mass are statistically representative along the central line. Thus, material inhomogeneities need not be resolved, and the moments of mass can be taken as constant. In an application problem, the beam's material properties can of course vary over certain regions, each of which is parameterized based on different calibrations. An appropriate transformation $\mathcal{T}$ can be found, for example, using Matlab's

Optimization Toolbox [51]. From here on, without loss of generality, we take $\mathcal{T}$ to be the identity map to avoid having to transform the vectorial and tensorial quantities needed for subsequent calculations. For a canonical reference configuration, the strain measures (18) become

$$\boldsymbol{\Gamma} = \boldsymbol{\Lambda}^T \mathbf{r}' - \boldsymbol{E}_3 \tag{23a}$$

$$\boldsymbol{\Omega} = \mathrm{ax}\big(\boldsymbol{\Lambda}^T \boldsymbol{\Lambda}'\big), \quad \widehat{\boldsymbol{\Omega}} = \boldsymbol{\Lambda}^T \boldsymbol{\Lambda}' \tag{23b}$$

3.3 Virtual deformation experiments

We now want to drive the atomistic system into a state as homogeneously deformed as possible. As will be shown in section 3.5, the generalized stress measures $\mathbf{n}, \mathbf{m}$ can be obtained from phase averages. Since these are approximated as time averages in MD, to properly sample phase space the atomic positions and momenta must be consistent with an isothermal (NVT) ensemble. In particular, the trajectories must be representative for the imposed kinematic state and thus must be allowed to freely explore the corresponding restricted phase space. The only constraint we apply is to prescribe positions for a set of boundary atoms $\partial\mathcal{A}_0 \subset \mathcal{A}_0$ at the free ends and, to produce sheared configurations, sometimes along thin stripes on the beam's lateral surface. In particular, we impose a pair of target strains $(\boldsymbol{\Gamma}_0, \boldsymbol{\Omega}_0)$ *exactly* at all boundary atoms $\overline{\boldsymbol{Q}}_i \in \partial\mathcal{A}_0$. These boundary displacements are applied slowly over time, starting at the initial positions $\overline{\boldsymbol{Q}}_i$ and finishing at end positions given by the target strain. In our simulations, this is carried out over 1 ns, followed by 1 ns of additional equilibration and finally 2 ns of actual sampling of the generalized stresses and strains in the now deformed state.

We derive the necessary displacements from the analytical description of a continuum system that is homogeneously deformed as $\boldsymbol{\Gamma}_0$ and $\boldsymbol{\Omega}_0$ everywhere. First, (23a) yields

$$\mathbf{r}'(S) = \boldsymbol{\Lambda}(S) \cdot (\boldsymbol{\Gamma}(S) + \boldsymbol{E}_3); \tag{24}$$

from (23b), we obtain

$$\boldsymbol{\Lambda}'(S) = \boldsymbol{\Lambda}(S) \cdot \widehat{\boldsymbol{\Omega}}(S). \tag{25}$$

For an initial central line position $\mathbf{r}_{\mathrm{in}}$ and an initial rotation $\boldsymbol{\Lambda}_{\mathrm{in}}$ at $S = 0$, we obtain a system of ordinary differential equations for $\mathbf{r}$ and $\boldsymbol{\Lambda}$:

$$\mathbf{r}'(S) = \boldsymbol{\Lambda}(S) \cdot (\boldsymbol{\Gamma}_0 + \boldsymbol{E}_3), \qquad \mathbf{r}(0) = \mathbf{r}_{\mathrm{in}} \tag{26a}$$

$$\boldsymbol{\Lambda}'(S) = \boldsymbol{\Lambda}(S) \cdot \widehat{\boldsymbol{\Omega}}_0, \qquad \boldsymbol{\Lambda}(0) = \boldsymbol{\Lambda}_{\mathrm{in}} \tag{26b}$$

Here, (26b) is uncoupled and immediately yields $\boldsymbol{\Lambda}(S) = \boldsymbol{\Lambda}_{\text{in}} \exp\big(S \cdot \widehat{\boldsymbol{\Omega}}_0\big)$. We can then integrate (26a) to obtain

$$\mathbf{r}(S) = \mathbf{r}_{\text{in}} + \boldsymbol{\Lambda}_{\text{in}} \left[\int_{s=0}^{S} \exp\big(s \cdot \widehat{\boldsymbol{\Omega}}_0\big)\, ds \right] \cdot (\boldsymbol{\Gamma}_0 + \boldsymbol{E}_3). \tag{27}$$

This integration can readily be carried out (Appendix A). For a beam whose end at $S = 0$ coincides with the canonical reference configuration we have $\mathbf{r}_0 = \mathbf{0}$ and $\boldsymbol{\Lambda}_0 = \boldsymbol{I}$. To facilitate subsequent parameter fitting, we are especially interested in pure strain states, where only one of the six strain components is non-zero. For example, pure bending about the x-axis, $\boldsymbol{\Gamma}_0 = [0, 0, 0]$, $\boldsymbol{\Omega}_0 = [\Omega_1, 0, 0]$, is described in component form as

$$\mathbf{r}(S) = \begin{bmatrix} 0 \\ \frac{1}{\Omega_1}(\cos(S \cdot \Omega_1) - 1) \\ \frac{1}{\Omega_1} \sin(S \cdot \Omega_1) \end{bmatrix}, \quad \boldsymbol{\Lambda}(S) = \begin{bmatrix} 1 & 0 & 0 \\ 0 & \cos(S \cdot \Omega_1) & -\sin(S \cdot \Omega_1) \\ 0 & \sin(S \cdot \Omega_1) & \cos(S \cdot \Omega_1) \end{bmatrix}. \tag{28}$$

Solutions for the remaining pure deformations are given in Appendix A. We have now identified the exact configuration that a continuum beam with a homogeneous strain would occupy. To obtain a candidate equilibrium state at finite temperature with approximately the same strain from an MD simulation, we must prescribe this configuration at the boundary particles of the atomistic beam. To induce a realistic deformation, we carry this out slowly over some time span t_e. The corresponding interpolation rules in time are given by:

$$\widehat{\mathbf{r}}(S,t) = \frac{1}{t_e}\big((t_e - t) \cdot \mathbf{R}(S) + t \cdot \mathbf{r}(S)\big) = \frac{t_e - t}{t_e} \cdot \begin{bmatrix} 0 \\ 0 \\ S \end{bmatrix} + \frac{t}{t_e} \cdot \mathbf{r}(S), \tag{29}$$

$$\widehat{\boldsymbol{\Lambda}}(S,t) = \boldsymbol{\Lambda}_0\big(\boldsymbol{\Lambda}_0^T \boldsymbol{\Lambda}(S)\big)^{\frac{t}{t_e}} = \boldsymbol{\Lambda}(S)^{\frac{t}{t_e}} \tag{30}$$

From these quantities we can set up the deformation mapping as

$$\widehat{\boldsymbol{\varphi}}(\boldsymbol{\zeta}, S, t) = \widehat{\mathbf{r}}(S,t) + \zeta^\alpha \widehat{\boldsymbol{d}}_\alpha(S,t), \tag{31}$$

with the directors $\widehat{\boldsymbol{d}}_\alpha$ extracted from $\widehat{\boldsymbol{\Lambda}}$. Now assume that an atom to be moved is initially at position $\boldsymbol{Q}$ and belongs to the continuum reference configuration, in which it has coordinates $\boldsymbol{\Phi}(\boldsymbol{\zeta}, S) = \boldsymbol{Q}$. The actual displacement of the atom[2] is therefore

$$\Delta\widehat{\boldsymbol{\varphi}}(\boldsymbol{\zeta}, S, t) := \widehat{\boldsymbol{\varphi}}(\boldsymbol{\zeta}, S, t) - \boldsymbol{\Phi}(\boldsymbol{\zeta}, S). \tag{32}$$

[2]In practice, the actual mean positions $\overline{\boldsymbol{Q}}$ of the boundary atoms are not deformed. Instead, their positions $\boldsymbol{Q}$ in the last timestep of the equilibration of the reference configuration are taken as the starting point.

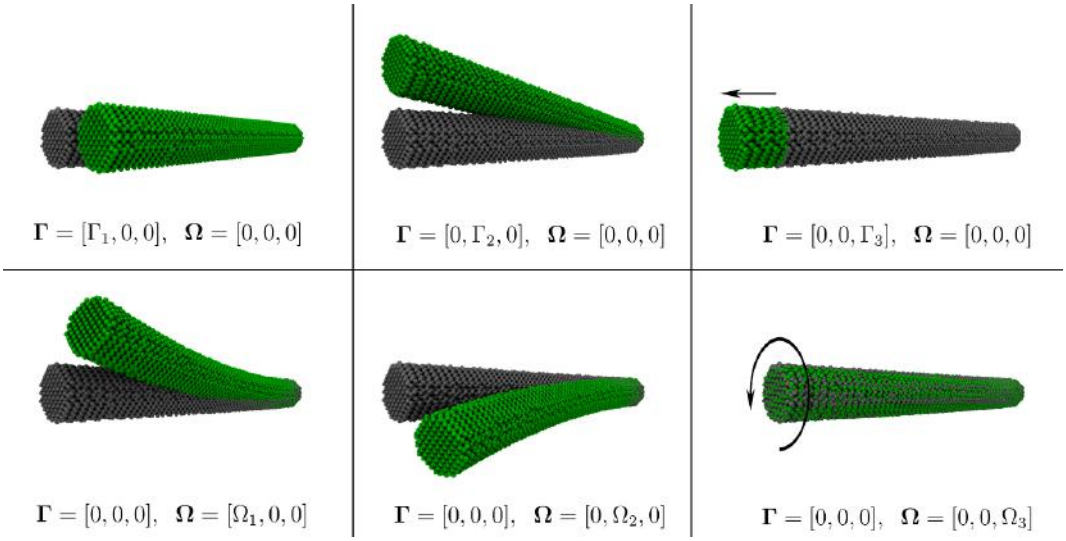

Figure 3: The six pure deformation modes of a geometrically exact beam, applied to an atomistic model of a nanowire.

Since the reference configuration is canonical, $(\zeta^1, \zeta^2, S) = (Q_1, Q_2, Q_3)$ and thus we can express the displacement in terms of the atomic coordinates,

$$\Delta\boldsymbol{\varphi}(\boldsymbol{Q}, t) := \Delta\widehat{\boldsymbol{\varphi}}(Q_1, Q_2, Q_3, t) = \widehat{\boldsymbol{\varphi}}(Q_1, Q_2, Q_3, t) - \boldsymbol{Q}. \tag{33}$$

which is suitable for implementation, as it can be evaluated for any given atomistic coordinate using (31). In figure 3, a sample nanowire is shown after being deformed to each of the six pure strain states. Finally, we note that prescribing positions for a boundary region $\partial\mathcal{A}_0$ does not cause the mean positions of the free-moving atoms to exactly attain those particular strain values. We merely impose the displacement to obtain candidates for deformed systems, from which we can determine the *actually* occurring local stresses and strains.

3.4 Generalized strain measures from atomistic simulations

Stresses and strains may be distributed non-homogeneously along the deformed beam. Therefore, we subdivide the beam along its arc length into a number of small segments $\mathcal{I}_j$, $j = 1, \ldots, N_{\text{seg}}$, of length $\Delta S = L/N_{\text{seg}}$. A sample nanowire with a highlighted segment is shown in figure 4. The set of atoms corresponding to segment j in the reference configuration is denoted $\mathcal{A}_{0,j}$. The new mean positions after deformation are called the *current* atomistic configuration:

$$\mathcal{A} = \{\, \bar{\boldsymbol{q}}_i \;\mid\; i = 1, \ldots, N \,\}, \quad \bar{\boldsymbol{q}}_i := \langle \boldsymbol{q}_i \rangle, \tag{34}$$

where the time average is taken after equilibration with the applied deformation boundary conditions. From the position changes of the atomic mean positions from $\overline{\boldsymbol{Q}}_i$ to $\bar{\boldsymbol{q}}_i$, $i \in \mathcal{A}_{0,j}$, we want to deduce the continuum strain measures $\boldsymbol{\Gamma}$ and $\boldsymbol{\Omega}$. To this end, we construct an approximation $\overline{\boldsymbol{\chi}}_j$ for the continuous deformation map $\boldsymbol{\chi}_j$ in segment j that interpolates the discrete displacement information by using the linear ansatz

$$\boldsymbol{q} = \boldsymbol{\chi}_j(\boldsymbol{Q}) \approx \overline{\boldsymbol{\chi}}_j(\boldsymbol{Q}) := \boldsymbol{F}_j \boldsymbol{Q} + \boldsymbol{c}_j \tag{35}$$

and determine $\boldsymbol{F}_j$ and $\boldsymbol{c}_j$ from the following least-squares problem [cf. 25]:

$$\frac{1}{2} \sum_{i \in \mathcal{A}_{0,j}} \left\| \overline{\boldsymbol{\chi}}_j(\overline{\boldsymbol{Q}}_i) - \bar{\boldsymbol{q}}_i \right\|^2 = \frac{1}{2} \sum_{i \in \mathcal{A}_{0,j}} \left\| \boldsymbol{F}_j \overline{\boldsymbol{Q}}_i + \boldsymbol{c}_j - \bar{\boldsymbol{q}}_i \right\|^2 \stackrel{!}{=} \min_{\boldsymbol{F}_j, \boldsymbol{c}_j}. \tag{36}$$

If atomic masses differ, a weighted cost function can be used. Similar choices for describing local atomic deformations are given in Horstemeyer and Baskes [52] and Zimmerman et al. [53, 54]. Since $\partial_{\boldsymbol{Q}} \boldsymbol{\chi}_j \approx \boldsymbol{F}_j$, the second-order tensor $\boldsymbol{F}_j$ plays the role of an approximate deformation gradient. From (7) and (10), the actual deformation gradient of a geometrically exact beam is given by

$$\boldsymbol{F}(\boldsymbol{\zeta}, S) = \boldsymbol{d}_1(S) \otimes \mathbf{E}^1 + \boldsymbol{d}_2(S) \otimes \mathbf{E}^2 + \boldsymbol{\varphi}'(\boldsymbol{\zeta}, S) \otimes \mathbf{E}^3. \tag{37}$$

Forming weighted averages of $\boldsymbol{d}_\alpha$ and $\mathbf{r}'$ over the beam segment domain $\mathcal{C} \times \mathcal{I}_j$ yields

$$\begin{aligned} \bar{\boldsymbol{d}}_\alpha := \langle \boldsymbol{d}_\alpha \rangle_{\mathcal{C}\times\mathcal{I}_j} &= \frac{\int_{\mathcal{C}\times\mathcal{I}_j} \boldsymbol{d}_\alpha(S) \rho_0(\boldsymbol{\zeta}, S)\, d\boldsymbol{\zeta} dS}{\int_{\mathcal{C}\times\mathcal{I}_j} \rho_0(\boldsymbol{\zeta}, S)\, d\boldsymbol{\zeta} dS} \\ &= \frac{\int_{\mathcal{I}_j} \boldsymbol{d}_\alpha(S) M_0(S)\, dS}{\int_{\mathcal{I}_j} M_0(S)\, dS} = \frac{1}{\Delta S} \int_{\mathcal{I}_j} \boldsymbol{d}_\alpha(S)\, dS \end{aligned} \tag{38a}$$

$$\bar{\mathbf{r}}' := \langle \mathbf{r}' \rangle_{\mathcal{C}\times\mathcal{I}_j} = \frac{\int_{\mathcal{C}\times\mathcal{I}_j} \mathbf{r}'(S) \rho_0(\boldsymbol{\zeta}, S)\, d\boldsymbol{\zeta} dS}{\int_{\mathcal{C}\times\mathcal{I}_j} \rho_0(\boldsymbol{\zeta}, S)\, d\boldsymbol{\zeta} dS} = \frac{1}{\Delta S} \int_{\mathcal{I}_j} \mathbf{r}'(S)\, dS, \tag{38b}$$

since M_0 is a constant along the entire calibration system. At the same time $M_1^\alpha \equiv 0$ and thus

$$\langle \zeta^\alpha \boldsymbol{d}'_\alpha \rangle_{\mathcal{C}\times\mathcal{I}_j} = \frac{\int_{\mathcal{C}\times\mathcal{I}_j} \boldsymbol{d}'_\alpha(S) \zeta^\alpha \rho_0(\boldsymbol{\zeta}, S)\, d\boldsymbol{\zeta} dS}{\int_{\mathcal{C}\times\mathcal{I}_j} \rho_0(\boldsymbol{\zeta}, S)\, d\boldsymbol{\zeta} dS} = \frac{\int_{\mathcal{I}_j} \boldsymbol{d}'_\alpha(S) M_1^\alpha(S)\, dS}{\int_{\mathcal{I}_j} M_0(S)\, dS} = \mathbf{0}. \tag{39}$$

Hence, the averaged deformation gradient follows from (37) as

$$\begin{aligned} \overline{\boldsymbol{F}}_j := \langle \boldsymbol{F} \rangle_{\mathcal{C}\times\mathcal{I}_j} &= \langle \boldsymbol{d}_1 \rangle_{\mathcal{C}\times\mathcal{I}_j} \otimes \mathbf{E}^1 + \langle \boldsymbol{d}_2 \rangle_{\mathcal{C}\times\mathcal{I}_j} \otimes \mathbf{E}^2 + \langle \mathbf{r}' + \zeta^\alpha \boldsymbol{d}'_\alpha \rangle_{\mathcal{C}\times\mathcal{I}_j} \otimes \mathbf{E}^3 \\ &= \bar{\boldsymbol{d}}_1 \otimes \mathbf{E}^1 + \bar{\boldsymbol{d}}_2 \otimes \mathbf{E}^2 + \bar{\mathbf{r}}' \otimes \mathbf{E}^3. \end{aligned} \tag{40}$$

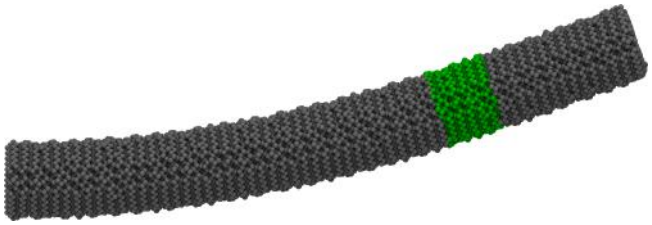

Figure 4: Silicon nanowire with a highlighted beam segment, indicating a particular selection of atoms.

Equating the least-squares deformation gradient $\boldsymbol{F}_j$ with (40) yields, in matrix form,

$$[\boldsymbol{F}_j] \stackrel{!}{=} \left[\overline{\boldsymbol{F}}_j\right] = \left[\bar{\boldsymbol{d}}_1, \bar{\boldsymbol{d}}_2, \overline{\mathbf{r}'}\right] \tag{41}$$

so the columns of $[\boldsymbol{F}_j]$ are just the averages of the directors and tangent vector of the central line defined above. Although the directors $\boldsymbol{d}_\alpha$ at specific locations $(\boldsymbol{\zeta}, S)$ are orthonormal, this need not hold for the averaged versions $\bar{\boldsymbol{d}}_\alpha$. However, we make this very assumption a priori and solve the minimization problem (36) under the constraint $\bar{\boldsymbol{d}}_\alpha \cdot \bar{\boldsymbol{d}}_\beta = \delta_{\alpha\beta}$. This is reasonable for relatively small beam segment lengths $\Delta S \approx 10\,\text{Å}$. This allows us to define a completed director basis for segment j as $\boldsymbol{\Lambda}_j := \left[\bar{\boldsymbol{d}}_1, \bar{\boldsymbol{d}}_2, \bar{\boldsymbol{d}}_3 = \bar{\boldsymbol{d}}_1 \times \bar{\boldsymbol{d}}_3\right]$. Using (23), the strain measures on beam segment j can be defined based on (40) as

$$\boldsymbol{\Gamma}_j := \boldsymbol{\Lambda}_j^T \overline{\mathbf{r}'} - \mathbf{E}_3, \tag{42}$$

$$\boldsymbol{\Omega}_j := \operatorname{ax}\left(\boldsymbol{\Lambda}_j^T \boldsymbol{\Lambda}_j'\right), \tag{43}$$

where the spatial derivative $\boldsymbol{\Lambda}_j'$ is obtained via ordinary finite differences, although this could be improved by a more suitable approximation scheme for orthogonal matrices.

3.5 Generalized stress measures from atomistic simulations

We still need to determine the forces $\mathbf{n}$ and moments $\mathbf{m}$ acting on cross sections of the beams from virtual deformation experiments. According to Simo [9], the following relationship holds:

$$\mathbf{n}(S) = \int_{\mathcal{C}} \boldsymbol{P}(\boldsymbol{\zeta}, S)\mathbf{E}_3 \, d\boldsymbol{\zeta} = \int_{\mathcal{C}} \boldsymbol{\sigma}(\boldsymbol{\zeta}, S)\boldsymbol{d}_3(S) \, d\boldsymbol{\zeta}, \tag{44}$$

where $\boldsymbol{P}$ is the first Piola-Kirchhoff stress and $\boldsymbol{\sigma}$ denotes the Cauchy stress, and the last equality follows from (37). We denote by $\mathbf{r}_j$ the centroid of deformed segment j and make the rather coarse approximations

$$\boldsymbol{\sigma}(\boldsymbol{\zeta}, S) \approx \boldsymbol{\sigma}(\mathbf{r}_j), \quad \boldsymbol{d}_3(S) \approx \bar{\boldsymbol{d}}_3 \tag{45}$$

throughout segment j. Hence (44) yields an approximate expression for the normal force in segment j:

$$\mathbf{n}_j := \int_{\mathcal{C}} \boldsymbol{\sigma}(\mathbf{r}_j)\bar{\boldsymbol{d}}_3 \, d\boldsymbol{\zeta} = R_{\mathrm{cs}}^2 \pi \cdot \boldsymbol{\sigma}(\mathbf{r}_j)\bar{\boldsymbol{d}}_3 \tag{46}$$

There are several methods for connecting the Cauchy stress to atomistic simulations [31]. To define a localized stress around the spatial point $\boldsymbol{x}$, a common approach is to use a virial stress expression such as

$$\boldsymbol{\sigma}^V(\boldsymbol{x}) = \frac{1}{\mathrm{vol}(\mathcal{N}_{\boldsymbol{x}})} \sum_{i \in \mathcal{N}_{\boldsymbol{x}}} \boldsymbol{\sigma}_i^V, \tag{47}$$

where $\mathcal{N}_{\boldsymbol{x}}$ is a suitable neighborhood of $\boldsymbol{x}$, and $\boldsymbol{\sigma}_i^V$ are the per-atom virial stresses of the atoms in this neighborhood, which involves the instantaneous particles' positions $\boldsymbol{q}_i$ and linear momenta $\boldsymbol{p}_i$ as well as the forces $\mathbf{f}_i$ acting on them, all of which appear in the time average at equilibrium:

$$\boldsymbol{\sigma}_i^V = \left\langle -\left(\frac{\boldsymbol{p}_i \otimes \boldsymbol{p}_i}{m_i} + \mathbf{f}_i \otimes \boldsymbol{q}_i \right) \right\rangle \tag{48}$$

Expression (47) for the stress tensor in three dimensions can be obtained by taking the derivative of (4) with respect to the state variable $\boldsymbol{F}$ [55]. We choose the set $\mathcal{A}_{,j}$ to be the neighborhood $\mathcal{N}_{\mathbf{r}_j}$ of $\boldsymbol{x} = \mathbf{r}_j$. This neighborhood spans the linearly transformed reference segment domain $\overline{\boldsymbol{\varphi}}_j(\mathcal{C} \times \mathcal{I}_j)$, $\overline{\boldsymbol{\varphi}}_j = \overline{\boldsymbol{\chi}}_j \circ \boldsymbol{\Phi}$, resulting in a volume of $R_{\mathrm{cs}}^2 \pi \cdot \Delta S \cdot \det \boldsymbol{F}_j$. Combining this with (46), we arrive at

$$\mathbf{n}_j = \frac{1}{\Delta S \cdot \det \boldsymbol{F}_j} \sum_{i \in \mathcal{A}_{0,j}} \boldsymbol{\sigma}_i^V \cdot \bar{\boldsymbol{d}}_3. \tag{49}$$

This gives us the first of two required generalized stress measures. The other is the moment acting on a cross section,

$$\mathbf{m}(S) = \int_{\mathcal{C}} (\boldsymbol{\varphi}(\boldsymbol{\zeta}, S) - \mathbf{r}(S)) \times \boldsymbol{\sigma}(\boldsymbol{\zeta}, S)\boldsymbol{d}_3(S) \, d\boldsymbol{\zeta} \tag{50}$$

$$= \int_{\mathcal{C}} \zeta^\alpha \boldsymbol{d}_\alpha(S) \times \boldsymbol{\sigma}(\boldsymbol{\zeta}, S)\boldsymbol{d}_3(S) \, d\boldsymbol{\zeta} \tag{51}$$

$$= \boldsymbol{d}_\alpha(S) \times \Big[\int_{\mathcal{C}} \zeta^\alpha \boldsymbol{\sigma}(\boldsymbol{\zeta}, S) \, d\boldsymbol{\zeta} \Big] \boldsymbol{d}_3(S). \tag{52}$$

To evaluate the integral in brackets, we partition the cross section into an overlapping grid of $N_h \times N_h$ smaller squares $\mathcal{C}_{(a,b)}$, each of side length $\Delta\zeta$ and with

midpoint $\boldsymbol{\zeta}_{(a,b)}$:

$$\int_{\mathcal{C}} \zeta^\alpha \boldsymbol{\sigma}(\boldsymbol{\zeta}, S)\, d\boldsymbol{\zeta} = \sum_{a=-N_h/2}^{N_h/2-1} \sum_{b=-N_h/2}^{N_h/2-1} \int_{\mathcal{C}_{(a,b)}} \zeta^\alpha \boldsymbol{\sigma}(\boldsymbol{\zeta}, S)\, d\boldsymbol{\zeta} \tag{53}$$

$$\doteq (\Delta\zeta)^2 \sum_{a=-N_h/2}^{N_h/2-1} \sum_{b=-N_h/2}^{N_h/2-1} \zeta^\alpha_{(a,b)} \boldsymbol{\sigma}^V\big(\boldsymbol{\zeta}_{(a,b)}, S\big) =: \mathbf{m}_j \tag{54}$$

In subsequent computations, we chose $N_h = 20$. Using (47) again, we evaluate $\boldsymbol{\sigma}^V\big(\boldsymbol{\zeta}_{(a,b)}, S\big)$ for a now smaller neighborhood $\mathcal{C}^V_{(a,b)} \times \mathcal{I}_j$, where $\mathcal{C}^V_{(a,b)}$ is a possibly different portion of the cross section used in the stress calculation:

$$\boldsymbol{\sigma}^V\big(\boldsymbol{\zeta}_{(a,b)}, S\big) = \frac{1}{\det \boldsymbol{F}_j \cdot \operatorname{area}\big(\mathcal{C}^V_{(a,b)}\big) \cdot \Delta S} \sum_{i \mid \overline{\boldsymbol{Q}}_i \in \boldsymbol{\Phi}\left(\mathcal{C}^V_{(a,b)} \times \mathcal{I}_j\right)} \boldsymbol{\sigma}^V_i \tag{55}$$

Finally, using (19), we obtain the corresponding material quantities

$$\mathbf{N}_j := \boldsymbol{\Lambda}_j^T \mathbf{n}_j, \quad \mathbf{M}_j := \boldsymbol{\Lambda}_j^T \mathbf{m}_j. \tag{56}$$

This and the preceding section provide the means that are necessary to bring in accordance the various quantities calculated for an equilibrated, deformed state of the atomistic beam with an assumed coinciding continuum beam. For the latter we can hence determine the local strains and stresses within each arc length segment $\mathcal{I}_j$.

3.6 Fitting of the energy density

We now must fit the energy density function, for which we make the quadratic ansatz

$$\psi(\boldsymbol{\Gamma}, \boldsymbol{\Omega}) = \frac{1}{2}\boldsymbol{\Gamma} \cdot \mathbf{C}_N \boldsymbol{\Gamma} + \frac{1}{2}\boldsymbol{\Omega} \cdot \mathbf{C}_M \boldsymbol{\Omega},$$

$$\mathbf{C}_N = \operatorname{diag}(GA_1, GA_2, EA), \tag{57}$$

$$\mathbf{C}_M = \operatorname{diag}(EI_1, EI_2, GJ), \tag{58}$$

where $\mathbf{C}_N$ contains shear stiffnesses and axial stiffness and $\mathbf{C}_M$ contains bending stiffnesses and torsional stiffness. We use the term "stiffness" for mere material-specific properties such as EA; in a different context it could in addition be divided by a geometric quantity such as the beam length. The resulting generalized stresses then have the form

$$\mathbf{N}(\boldsymbol{\Gamma}, \boldsymbol{\Omega}) = \partial_{\boldsymbol{\Gamma}} \psi(\boldsymbol{\Gamma}, \boldsymbol{\Omega}) = \mathbf{C}_N \boldsymbol{\Gamma}, \tag{59a}$$

$$\mathbf{M}(\boldsymbol{\Gamma}, \boldsymbol{\Omega}) = \partial_{\boldsymbol{\Omega}} \psi(\boldsymbol{\Gamma}, \boldsymbol{\Omega}) = \mathbf{C}_M \boldsymbol{\Omega}. \tag{59b}$$

Though simple, this completely uncoupled choice for the stress-strain relationship has proven very useful and is employed throughout the literature [40]. Of course, more elaborate functional forms can be used without affecting the essential fitting procedure. For general materials, however, about which we have no prior information on additional deformation modes, a quadratic energy function typically is a suitable guess. Even for large beam deflections, the local stress-strain relationship can usually be well approximated as linear. If additional knowledge on the material at hand is available and a suitably adapted energy function is known, it can be fitted in the same manner. In these cases, however, new VDEs should be introduced to trigger the additional modes, as in section 3.3.

The procedures described in sections 3.4 and 3.5, yield material stress-strain quadruples $\left(\mathbf{\Gamma}_j^{(k)}, \mathbf{\Omega}_j^{(k)}, \mathbf{N}_j^{(k)}, \mathbf{M}_j^{(k)}\right)$ for each segment and for a larger set of virtual deformation experiments (VDE) with index $k = 1, \ldots, N_{\text{vde}}$. If we arrange the six unknown material properties from (58) as a vector $\boldsymbol{\lambda} \in \mathbb{R}^6$ we obtain the following objective function to fit these unknowns:

$$g(\boldsymbol{\lambda}) := \frac{1}{2} \sum_{k=1}^{N_{\text{vde}}} \sum_{j=1}^{N_{\text{seg}}} \Big(\left\| \mathbf{N}_j^{(k)} - \mathbf{N}(\mathbf{\Gamma}_j^{(k)}, \mathbf{\Omega}_j^{(k)}) \right\|^2 + \left\| \mathbf{M}_j^{(k)} - \mathbf{M}(\mathbf{\Gamma}_j^{(k)}, \mathbf{\Omega}_j^{(k)}) \right\|^2 \Big) \tag{60}$$

$$= \frac{1}{2} \sum_{k=1}^{N_{\text{vde}}} \sum_{j=1}^{N_{\text{seg}}} \Big(\left\| \mathbf{N}_j^{(k)} - \mathbf{C}_N \mathbf{\Gamma}_j^{(k)}) \right\|^2 + \left\| \mathbf{M}_j^{(k)} - \mathbf{C}_M \mathbf{\Omega}_j^{(k)}) \right\|^2 \Big) \tag{61}$$

Minimization of g yields the sought material-specific stiffnesses. Since the partial derivatives of ψ are fully decoupled and since, by construction of the virtual experiments, we expect only one component of $(\mathbf{\Gamma}, \mathbf{\Omega})$ to deviate significantly from zero, it makes sense to fit each parameter λ_i individually: for example,

$$g(EA) = g(\lambda_3) = \frac{1}{2} \sum_k \sum_j \Big(N_{j,3}^{(k)} - \lambda_3 \, \Gamma_{j,3}^{(k)} \Big)^2 \tag{62}$$

By eliminating the noise in the remaining stress and strain components the value of the final fitted parameter can usually be stabilized. Here, k runs only over those VDEs designed to excite the corresponding deformation mode.

4 Numerical results

We now present, as a benchmark, a direct comparison between purely atomistic and continuum mechanical simulations. We do not distinguish between calibration and full system; material parameters are determined for the same system size used for the benchmark calculations. The MD simulations have been performed using LAMMPS [56], while the finite element code for the beam model

has been implemented based on the libMesh library [57]. Specifically, for a silicon nanowire and a carbon nanotube we perform $N_{\mathrm{vde}} = 30$ virtual experiments with strain components $\Gamma_i = 0.02, 0.04, \ldots, 0.10$ and $\Omega_i = 2 \times 10^{-4}\,\text{Å}^{-1}$, $5 \times 10^{-4}\,\text{Å}^{-1}$, $8 \times 10^{-4}\,\text{Å}^{-1}$, $0.001\,\text{Å}^{-1}$, $0.002\,\text{Å}^{-1}$ for $i = 1, 2, 3$. These choices are representative as guidelines for the choice of VDEs. The values of Γ_i and Ω_i should be restricted to the range of deformations that can be represented by the chosen functional form for the energy density ψ. In the case of (58) this means that the stress-strain relationship should remain linear. A possibly larger range may be included when a nonlinear relationship is assumed. By inspection of the input data generated by the VDEs one can exclude cases that cannot be properly captured by the chosen functional form.

Furthermore, we usually exclude some beam segments close to the boundary where atom positions are fixed and computed stresses are not meaningful. We also note that a simple hyperelastic material model like (58) can only be fitted to a certain range of deformations, as dictated by the virtual deformation experiments used, though extensions to overcome this issue could be conceived.

4.1 Contact with a Lennard-Jones wall

An atomistic beam is initially aligned along the z-axis from $X_3 = 0$ to $X_3 = L$. A small set $\partial\mathcal{A}_0$ of atoms near the origin is kept fixed. We then introduce a half-space E^- of Lennard-Jones (LJ) particles separated from the beam by a plane E with outer unit normal $\boldsymbol{\nu} \in \mathbb{R}^3$ and distance $-d$ from the origin. The half-space containing the LJ particles is then given by

$$E^- = \big\{\boldsymbol{y} \in \mathbb{R}^3 \mid \boldsymbol{y} \cdot \boldsymbol{\nu} - d < 0\big\}, \tag{63}$$

while the beam and origin are located in the complementary half-space

$$E^+ = \big\{\boldsymbol{y} \in \mathbb{R}^3 \mid \boldsymbol{y} \cdot \boldsymbol{\nu} - d > 0\big\}. \tag{64}$$

The distance $d_E(\boldsymbol{y}) = \boldsymbol{y}\cdot\boldsymbol{\nu} - d$ partitions $\mathbb{R}^3$ into E, E^-, and E^+. Although infinite, E^- can be seen as a good approximation to a large rigid body that interacts with the beam via a LJ potential. As it is not itself deformed, E^- is is not an explicit part of our model; only its interactions with the beam are. The wall can be pushed towards the beam, which is still fixed at one end, as shown in fig. 5. Thus d increases over multiple displacement steps. As a result, the beam undergoes a substantial deflection away from the wall but always remains in E^+. The potential energy of the entire wall interacting with a particle at position $\boldsymbol{x} \in E^+$ is an infinite sum over all pairwise LJ interactions, which have the form:

$$\phi(r) = 4\widetilde{\varepsilon}\left[\left(\frac{\sigma}{r}\right)^{12} - \left(\frac{\sigma}{r}\right)^{6}\right] \tag{65}$$

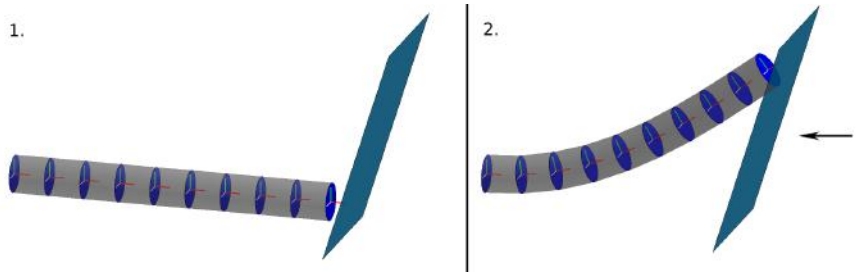

Figure 5: Illustration of a geometrically exact beam, 1. in its undeformed reference configuration and 2. after coming into contact with a rigid Lennard-Jones wall.

Similar to [58], we approximate this summation through an integral over a continuum of LJ sites with constant particle density $\widehat{\beta}_w$,

$$\pi_w(\boldsymbol{x}) = \int_{E^-} \widehat{\beta}_w \cdot \phi(\|\boldsymbol{y} - \boldsymbol{x}\|)\, d\boldsymbol{y} \tag{66}$$

$$= \underbrace{\frac{2}{3}\pi\widehat{\beta}_w\widetilde{\varepsilon}\sigma^3}_{=:\varepsilon}\left[\frac{2}{15}\left(\frac{\sigma}{d_E(\boldsymbol{x})}\right)^9 - \left(\frac{\sigma}{d_E(\boldsymbol{x})}\right)^3\right] = \phi_{93}(\, d_E(\boldsymbol{x})\,), \tag{67}$$

resulting in the so-called Lennard Jones 9-3 potential

$$\phi_{93}(d_E) = \varepsilon\left[\frac{2}{15}\left(\frac{\sigma}{d_E}\right)^9 - \left(\frac{\sigma}{d_E}\right)^3\right], \tag{68}$$

which is a function only of the distance d_E of the particle from plane E. These interactions can be easily modeled using LAMMPS.

We now turn to the continuum framework and determine the total interaction energy between this wall and a deformed configuration $\boldsymbol{\varphi}$ of the geometrically exact beam. To this end, we introduce the *contact* energy, which weights all particle interactions with the wall by the current particle density of the beam, $\widehat{\beta}(\boldsymbol{x})$:

$$\Pi_c[\boldsymbol{\varphi}] = \int_{\mathcal{B}} \widehat{\beta}(\boldsymbol{x})\, \pi_w(\boldsymbol{x})\, d\boldsymbol{x} = \int_{\mathcal{C}}\int_{\mathcal{I}} \widehat{\beta}(\boldsymbol{\varphi}(\boldsymbol{\zeta}, S))\, \pi_w(\boldsymbol{\varphi}(\boldsymbol{\zeta}, S))\, |\det D\boldsymbol{\varphi}(\boldsymbol{\zeta}, S)|\, d\boldsymbol{\zeta} dS \tag{69}$$

We define the transformed particle density

$$\beta(\boldsymbol{\zeta}, S) := \widehat{\beta}(\boldsymbol{\varphi}(\boldsymbol{\zeta}, S))\, |\det D\boldsymbol{\varphi}(\boldsymbol{\zeta}, S)| = \widehat{\beta}_0(\boldsymbol{\Phi}(\boldsymbol{\zeta}, S)) \tag{70}$$

and make the simplifying assumption for the reference particle density $\widehat{\beta}_0(\boldsymbol{X})$ that $\partial_{X_\alpha}\widehat{\beta}_0 \equiv 0$, $\alpha = 1, 2$, yielding $\beta = \beta(S)$ and hence

$$\Pi_c[\boldsymbol{\varphi}] = \int_{\mathcal{I}} \beta(S) \int_{\mathcal{C}} \pi_w(\mathbf{r}(S) + \zeta^\alpha \boldsymbol{d}_\alpha(S))\, d\boldsymbol{\zeta}\, dS. \tag{71}$$

We can evaluate the inner integral of (71) analytically at a specific arc-length position S:

$$\int_{\mathcal{C}} \pi_w(\mathbf{r}+\zeta^\alpha \boldsymbol{d}_\alpha)\, d\boldsymbol{\zeta} = \frac{2}{15}\varepsilon\sigma^9 \int_{\mathcal{C}} d_E(\mathbf{r}+\zeta^\alpha \boldsymbol{d}_\alpha)^{-9}\, d\boldsymbol{\zeta} - \varepsilon\sigma^3 \int_{\mathcal{C}} d_E(\mathbf{r}+\zeta^\alpha \boldsymbol{d}_\alpha)^{-3}\, d\boldsymbol{\zeta} \tag{72}$$

$$= \frac{2}{15}\varepsilon\sigma^9 \cdot J_9(d_E(\mathbf{r}), \boldsymbol{\nu}\cdot\mathbf{Q}\boldsymbol{d}_1, R_{\mathrm{cs}}) - \varepsilon\sigma^3 \cdot J_3(d_E(\mathbf{r}), \boldsymbol{\nu}\cdot\mathbf{Q}\boldsymbol{d}_1, R_{\mathrm{cs}}), \tag{73}$$

for an appropriately chosen[3] orthogonal transformation $\mathbf{Q}$ and

$$J_9(a,b,R) = \frac{R^2\pi}{64}\cdot\frac{5b^6R^6 + 120a^2b^4R^4 + 240a^4b^2R^2 + 64a^6}{(a-Rb)^{15/2}(a+Rb)^{15/2}}, \tag{74}$$

$$J_3(a,b,R) = \frac{R^2\pi}{(a-Rb)^{3/2}(a+Rb)^{3/2}}. \tag{75}$$

The details of this calculation are deferred to B. A similar procedure might also be feasible to find a closed-form expression for the LJ interaction between two circular cross sections, which could be used to simplify the computation of the contact energy between two beams. If the assumption $\beta(\boldsymbol{\zeta}, S) \equiv \beta(S)$ is violated, the relationship (71) can be generalized straight-forwardly if the particle density β is piecewise constant within a number N_{ann} of concentric annuli of radii $0 = R_{\mathrm{cs},0} < R_{\mathrm{cs},1} < \cdots < R_{\mathrm{cs},N_{\mathrm{ann}}} = R_{\mathrm{cs}}$. In this case, the integral over a single annulus is obtained by subtracting the expression for a disk with radius $R_{\mathrm{cs},i-1}$ from that for $R_{\mathrm{cs},i}$. On the other hand, the continuum problem that we want to solve is to minimize the energy functional

$$\Pi[\boldsymbol{\varphi}] := \Pi_{\mathrm{int}}[\boldsymbol{\varphi}] + \Pi_c[\boldsymbol{\varphi}], \quad \Pi_{\mathrm{int}}[\boldsymbol{\varphi}] := \int_{\mathcal{I}} \psi\big(\boldsymbol{\Gamma}[\boldsymbol{\varphi}](S), \boldsymbol{\Omega}[\boldsymbol{\varphi}](S)\big)\, dS, \tag{76}$$

subject to fixed boundary conditions at $S = 0$. The relevant thermodynamic potential for isothermal conditions is the Helmholtz free energy, whose internal part is given by Π_{int}. Π_c actually denotes only the potential energy of the wall–beam interaction, since it seems unfeasible to devise a proper model for the free energy of the interaction with a wall (given in terms of $\boldsymbol{\nu}$ and d). We therefore consider Π_c as a suitable approximation for the latter.

We now carry out a fully atomistic simulation of a beam interacting with an approaching LJ wall. At equilibrium, we extract certain quantities of interest and compare them to their continuum equivalents obtained from finite element

[3]See B. The symbol $\mathbf{Q}$ for the orthogonal transformation is not to be confused with the atomic positions.

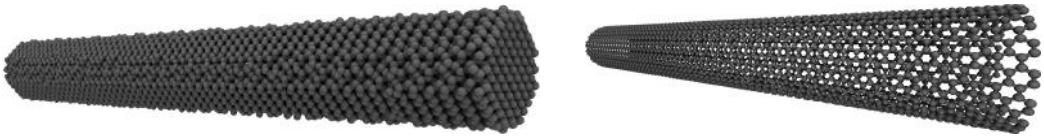

(a) (b)

Figure 6: Snapshot of (a) an undeformed silicon nanowire and (b) an undeformed carbon nanotube.

calculations of an analogous quasi-static process. In this way, we can assess the accuracy with which the surrogate model reproduces the "exact" MD values. We study two such quantities here. First, we consider the total force of the wall exerted on the beam. This is expressed for the atomistic case as the time-average

$$\boldsymbol{f}_{\text{at}} = \left\langle -\boldsymbol{\nu} \sum_{i=1}^{N} \phi'_{93}(d_E(\boldsymbol{q}_i)) \right\rangle, \tag{77}$$

while the continuum version can be obtained by differentiating Π_c:

$$\boldsymbol{f}_{\text{cont}} = -\boldsymbol{\nu}\, \varepsilon \int_{\mathcal{I}} \beta \Big[\frac{2}{15} \sigma^9 \cdot \partial_a J_9(d_E(\mathbf{r}), \boldsymbol{\nu} \cdot \mathbf{Q}\boldsymbol{d}_1, R_{\text{cs}}) - \sigma^3 \cdot \partial_a J_3(d_E(\mathbf{r}), \boldsymbol{\nu} \cdot \mathbf{Q}\boldsymbol{d}_1, R_{\text{cs}}) \Big]\, dS, \tag{78}$$

where $\mathbf{r} = \mathbf{r}(S)$, $\boldsymbol{Q} = \boldsymbol{Q}(S)$ and $\boldsymbol{d}_1 = \boldsymbol{d}_1(S)$ in the integrand all depend on S. As expected, the forces are in both cases directed along the wall normal vector $\boldsymbol{\nu}$. Secondly, we compute the eccentricity, or the deflection of the central line's right-hand end $\mathbf{r}(L)$ from the z-axis, on which it lies in the reference configuration:

$$\sqrt{r_1(L)^2 + r_2(L)^2}. \tag{79}$$

4.2 Results for Silicon Nanowires

The first system of interest are so-called nanowires, which are crystalline metallic or metalloid, slender objects with a small radius compared to their length (figure 6a). Nanowires have numerous potential applications, such as nano-electronics, nanosensors and photonics [1]. The numerical studies in this work are carried out for Si nanowires, where the interatomic interactions are described through a Stillinger-Weber potential [59]. The mechanical behavior of silicon nanowires (SiNW) has frequently been studied using both atomistic simulations [60] and experiments [61, 62].

The nanowire systems studied here have lengths between $L_g = 50a$ and $L_g = 150a$, where $a = 5.431\,\text{Å}$ is the lattice constant of Si. L_g denotes the "geometric" length of the crystalline starting configuration used in the MD simulations. Due

to thermal fluctuations, the atomistic reference configuration $\mathcal{A}_0$ typically deviates from this perfectly straight shape, leading to different effective lengths L. Three cross sections were chosen as circular (001) surfaces with atoms located within different radii of $R_{\mathrm{g}} = 2.5a$, $R_{\mathrm{g}} = 3.5a$ and $R_{\mathrm{g}} = 4.5a$, which are also merely geometric. Physically, though, the atoms are not point particles, but have a finite extent; for example, the van der Waals radius of Si is $R_{\mathrm{vdw}} = 2.1\,\text{Å}$. Therefore, the effective cross-sectional radius is $R_{\mathrm{cs}} = R_{\mathrm{g}} + R_{\mathrm{vdw}}$. The Lennard-Jones parameters of the wall interaction were set to $\varepsilon = 600\,\text{Å}^3\,\text{bar}$ and $\sigma = 3.5\,\text{Å}$, and the wall was tilted against the z-axis, $\boldsymbol{\nu} = \left[0, 0.3, -\sqrt{0.91}\right]^T$.

The identified mass-dependent properties for systems of different radius and length are summarized in table 1. The temperature was always $T = 300\,\text{K}$. We see that the inertia is distributed symmetrically, as expected. The only exception is the very slender nanowire ($R_{\mathrm{g}} = 2.5a$, $L_g = 150a$), where the thermal vibrations lead to significant deviations in the atomic mean positions from a canonical reference configuration even without any deforming boundary conditions applied, resulting in a seemingly asymmetric mass distribution. Averaging the atom positions over a longer time span may attenuate this issue. The material parameters determined for the constitutive law (58) are presented in table 2.

R_{g}	L_g	L [Å]	M_0 [Å^{-1} u]	M_2^{11} [Å u]	M_2^{22} [Å u]
$2.5a$	$50a$	266	853	40 300	40 700
$2.5a$	$150a$	798	851	52 000	41 300
$3.5a$	$60a$	327	1580	141 000	141 000
$3.5a$	$150a$	814	1580	141 000	141 000
$4.5a$	$150a$	813	2640	394 000	394 000

Table 1: Silicon nanowires: The identified effective length L, mass density M_0 and cross section inertia $M_2^{\alpha\alpha}$, for various geometric dimensions R_{g}, L_g. Remark: 1 u $= 1.66 \times 10^{-27}\,\text{kg}$.

R_{g}	L_g	GA_1 [Å^{2}bar]	GA_2 [Å^{2}bar]	EA [Å^{2}bar]	EI_1 [Å^{4}bar]	EI_2 [Å^{4}bar]	GJ [Å^{4}bar]
$2.5a$	$50a$	2.37×10^8	2.29×10^8	4.09×10^8	1.86×10^{10}	1.87×10^{10}	2.00×10^{10}
$2.5a$	$150a$	1.75×10^8	1.68×10^8	3.84×10^8	1.67×10^{10}	1.83×10^{10}	1.80×10^{10}
$3.5a$	$60a$	4.67×10^8	4.66×10^8	9.31×10^8	7.60×10^{10}	7.76×10^{10}	9.02×10^{10}
$3.5a$	$150a$	4.70×10^8	4.62×10^8	9.67×10^8	6.86×10^{10}	7.39×10^{10}	8.84×10^{10}
$4.5a$	$150a$	8.34×10^8	8.27×10^8	1.58×10^9	2.25×10^{11}	2.02×10^{11}	2.61×10^{11}

Table 2: Silicon nanowires: The identified material parameters for the constitutive law (58), for various geometric dimensions R_{g}, L_g. Remark: $1\,\text{Å}^2$ bar $= 10^{-15}\,\text{N}$, $1\,\text{Å}^4$ bar $= 10^{-35}\,\text{Nm}^2$.

p_d	GA_1 [Å^{2}bar]	GA_2 [Å^{2}bar]	EA [Å^{2}bar]	EI_1 [Å^{4}bar]	EI_2 [Å^{4}bar]	GJ [Å^{4}bar]
0%	4.67×10^8	4.66×10^8	9.31×10^8	7.60×10^{10}	7.76×10^{10}	9.02×10^{10}
1%	4.75×10^8	4.64×10^8	8.50×10^8	6.69×10^{10}	7.30×10^{10}	7.99×10^{10}
2%	4.25×10^8	4.23×10^8	7.55×10^8	6.23×10^{10}	5.72×10^{10}	7.12×10^{10}

Table 3: Silicon nanowires: The identified material parameters for the constitutive law (58) for a system with $L_g = 60a$, $R_{\mathrm{g}} = 3.5a$ and vacancy percentages p_d of removed atoms.

Dividing the axial stiffness EA by the cross-sectional area $A = R_{\mathrm{cs}}^2\pi$ gives the axial Young's modulus of the beam. For example, for beams of length $L_g = 150a$ and radii $R_{\mathrm{g}} = 2.5a$, $3.5a$, and $4.5a$ we find $E = 49.8\,\mathrm{GPa}$, $69.1\,\mathrm{GPa}$, and $71.3\,\mathrm{GPa}$, respectively. These values are significantly smaller than Young's modulus for bulk Si, which is $151.4\,\mathrm{GPa}$ for the Stillinger-Weber potential. This reveals a well-known size effect in the mechanical properties of nanowires, caused by non-negligible surface effects as the surface-to-volume ratio becomes large [63–66]. Thus, without a rule for scaling the material properties between different radii (and possibly different cross-sectional shape), one has to repeat the parameter identification procedure for each type of cross section.

The structures considered so far were constructed in a perfectly defect-free manner. In reality, though, there is usually a certain amount of defects present in the system. We can take this into account by identifying material parameters that reflect a given statistical distribution of such defects. To this end, one can for example build an initial configuration that contains vacancies, impurities etc. in a prescribed amount. The size of the calibration system then needs to be chosen large enough such that it constitutes a representative sample of defect distribution. Like before, one has to keep in mind that the continuum material description cannot capture plastic events. As the latter may be triggered more easily in the presence of defects, the material parameters determined may only be valid for relatively small local strains.[4] Table 3 shows the material parameters found for again a SiNW at $T = 300\,\mathrm{K}$ with geometric dimensions $L_g = 60a$ and $R_{\mathrm{g}} = 3.5a$, but this time with vacancy ratios $p_d = 0\%$, 1% and 2%. That is, a percentage p_d of atoms are randomly removed from the perfect nanobeam, followed by the usual conducting of the VDEs. The table demonstrates how the structural weakening can be quantified as more vacancies lead to a consistent decrease in the stiffness values.

Figure 7 shows the y- and z-components of the force exerted by the LJ wall onto the beam over a displacement range of $35\,\mathrm{Å}$, where a displacement of zero

[4] In principle, within a concurrent multiscale method, one could alternatively also use a two-level approach that solves a microscale problem around each point defect [67].

corresponds to the wall having moved to the initial location of the free end of the beam's central line; an increasing value means that the wall has moved beyond this point to cause more deflection. Each of the eighty displacement steps consisted of 0.4 ns of moving the wall by a small increment, another 0.4 ns of equilibration and 0.4 ns of sampling. The shift between the continuum and atomistic curve is chosen to yield good visual agreement; this implicitly determines the effective reach of the continuum beam within this contact problem. Error bars in the plot indicate the standard deviation of ten repeated MD simulations, each performed with a varying perturbation in the initial atomic velocities. We see that the trends of the forces are well captured by the continuum model, where they remain within one standard deviation from the atomistic mean values. However, we notice that the continuum forces contain a mild level of consistent underprediction with respect to the MD values. The error bars also show the fluctuation in the time-averaged atomistic forces increases as the wall approaches the beam. This can be explained by the increasing number of beam atoms that interact with the wall, as each particle introduces additional thermal fluctuations to the force (77). Also note that due to (77), (78) the two graphs are related to each other and differ only by the scaling of different components of $\boldsymbol{\nu}$. An enlarged image detail of the adhesive regime of the forces in y-direction is provided in figure 8.

The eccentricity, or the deflection of the beam's end from the z-axis, is shown in figure 9 over a displacement range of 70 Å. We still see qualitiative agreement, though the deflection is overestimated by the continuum model. The error bars are omitted since there is little variation in the atomistic data. To extract the beam's geometry in each displacement step, we proceed as in section 3.4. For the same displacement range, the corresponding forces are shown in figure 10.

4.3 Results for Carbon Nanotubes

As a second test case, we study single-walled carbon nanotubes (CNT) as shown in figure 6b. Due to their remarkable properties and their potential applications, CNTs have been thoroughly investigated in recent decades both experimentally [68–70] and via modeling. Mechanical properties such as the elastic modulus and bending stiffness can be found from atomistic models [71]. Significant effort has been expended to represent CNTs through specialized continuum models such as Euler-Bernoulli [72, 73] and Timoshenko [74, 75] beams, and in particular to study buckling behavior [76–78]. Moreover, [79] uses a nonlocal Euler-Bernoulli beam and a cylindrical shell description to predict the critical buckling strains of nanotubes. Finite-temperature simulations of a continuum based on the local harmonic approximation have also been performed [22].

Gould and Burton [80] and Fang et al. [18] have also successfully modelled CNTs by extending the classical Cosserat theory to allow cross-sectional deforma-

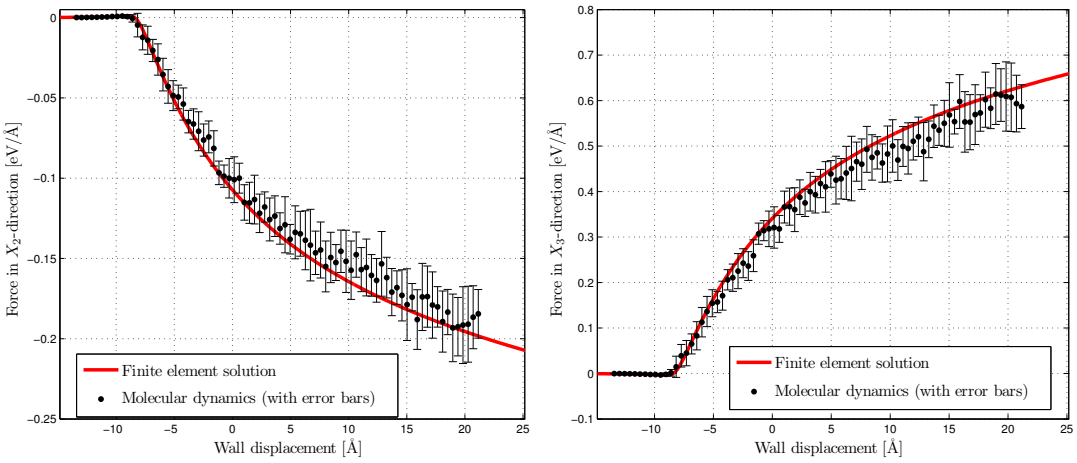

(a) (b)

Figure 7: Silicon nanowire ($R_{\mathrm{cs}} = 3.5a$, $L_g = 60a$): Forces exerted on the beam structure by a moving Lennard-Jones wall, which gets closer at increasing displacements. Error bars indicate the standard deviation. Remark: $1\,\mathrm{eV\,Å^{-1}} = 1.6022\,\mathrm{nN}$.

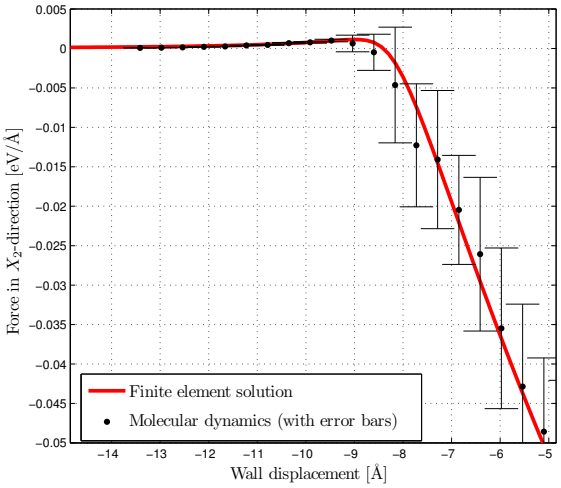

Figure 8: Silicon nanowire ($R_{\mathrm{cs}} = 3.5a$, $L_g = 60a$): Enlargement of the forces from figure 7a.

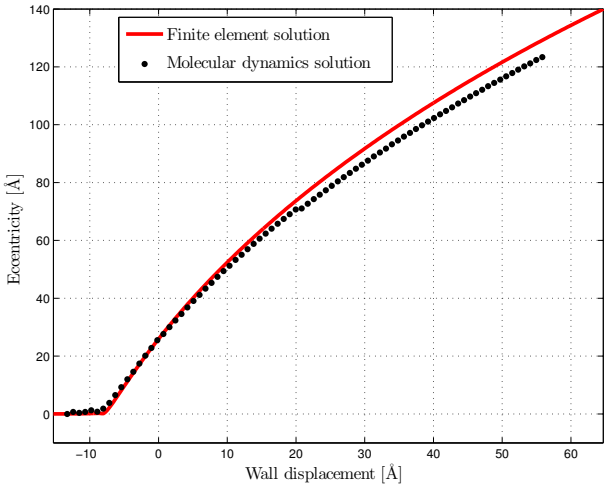

Figure 9: Silicon nanowire ($R_{\mathrm{cs}} = 3.5a$, $L_g = 60a$): Deflection of the beam's free end from the z-axis over an increased displacement range of 70 Å.

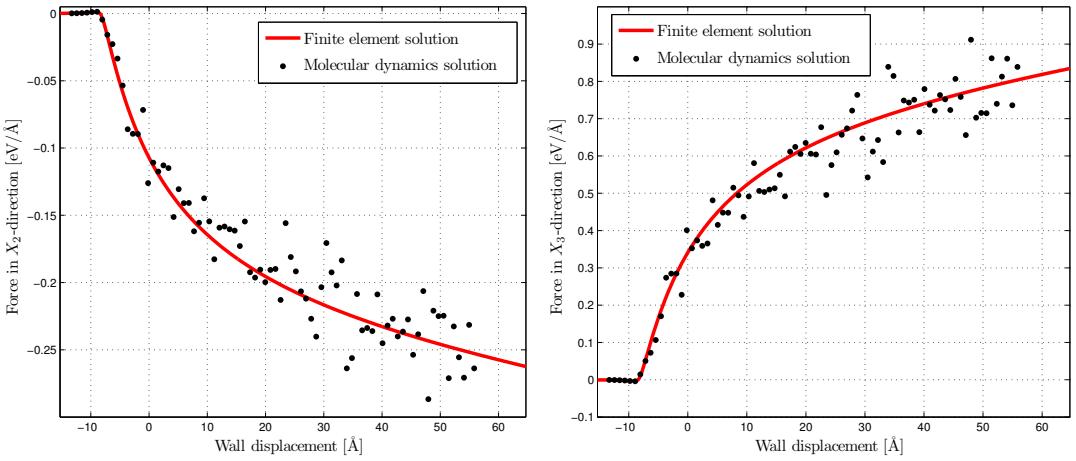

(a) (b)

Figure 10: Silicon nanowire ($R_{\mathrm{cs}} = 3.5a$, $L_g = 60a$): Forces exerted on the beam structure by a moving Lennard-Jones wall, over a larger displacement range of 70 Å.

tions of tubular systems. The work of Chandraseker et al. [17] is quite similar to ours in that CNTs are deformed by imposing boundary conditions on the outermost atoms, then minimizing the structure's energy and finally using the atomic positions to determine the strain measures to fit an energy density function. The energies are based on DFT calculations and therefore neglect thermal effects.

Due to their tubular structure, another natural way to model CNTs as continua is to take its shell- or sheet-like character directly into account [81–83]. Arroyo and Belytschko [12] have developed the exponential Cauchy-Born rule for membrane structures and apply it in finite element simulations of single- and multi-walled CNTs, also in problems involving buckling. Zhang et al. [84] use Cosserat surfaces and an especially adapted variant of the CBR to determine the material behavior. Zhang et al. [85] and Hollerer [86] have also used a coupled atomistic-continuum approach.

Our atomistic simulations are based on a Tersoff potential for the carbon bonds [87]. Outside of the Tersoff cutoff of 2.1 Å, van der Waals interactions are added through an additional LJ potential with $\varepsilon_{\mathrm{CC}} = 2.39\,\mathrm{meV}$, $\sigma_{\mathrm{CC}} = 3.41\,\text{Å}$ [88, 89] and a cutoff radius of $2.5\sigma_{\mathrm{CC}}$. The geometry of a CNT is specified by a pair of indices (n, m). Suitable initial configurations can be generated with software like VMD [90] or Nanocap [91]. Here we consider $(n, m) = (10, 10)$, $(15, 15)$, $(20, 20)$ and $(25, 25)$, resulting in so-called armchair configurations, with a geometric radius of

$$R_{\mathrm{g}} = \frac{c}{2\pi}\sqrt{m^2 + mn + n^2} \quad (c = 2.46\,\text{Å}). \tag{80}$$

[92]. To this, the van der Waals radius $R_{\text{vdw}} = 1.7\,\text{Å}$ for C is added to obtain R_{cs}. The effective length of the systems was about 380 Å for the three smaller cross sections and 492.67 Å for the $n = m = 25$ case. Furthermore, the temperature was again kept at $T = 300\,\text{K}$ and the LJ parameters of the wall interaction were set to $\varepsilon = 10\,000\,\text{Å}^3\,\text{bar}$, $\sigma = 2.5\,\text{Å}$; $\boldsymbol{\nu}$ remains as above, too.

For the four systems, we present the computed mass-related quantities in table 4, and the corresponding parameters for the constitutive law in table 5. For the CNTs with $n = m = 10, 15, 20, 25$ we find the following axial Young's moduli: $E = 643\,\text{GPa}$, 543 GPa, 426 GPa and 377 GPa. These quantities agree with data reported in the literature [3, 93–95], where a range between 300 GPa and 1 TPa is typically found. The axial shear modulus can be found by dividing the torsional stiffness GJ by the polar moment of area $J = R_{\text{cs}}^4\pi/2$. We obtain values of $G = 578\,\text{GPa}$, 501 GPa, 405 GPa and 364 GPa, respectively, which is also consistent with other simulations [96, 97].

We can also have another look at how the material behavior changes under variations in the temperature. For the $(20, 20)$ system, the values corresponding to $T = 300\,\text{K}$, 450 K, 600 K and 750 K are shown in table 6. Additional material parameters have also been identified for the case that a certain vacancy percentage p_d is introduced. Results for the $(15, 15)$ system with vacancies are listed in table 7. Like before in the SiNW setting, a monotonous decrease of all stiffnesses can be observed.

In figure 11, we see the y- and z-components of forces exerted on the $(15, 15)$ CNT by the LJ wall as it is displaced 40.0 Å. Again we observe good agreement between the atomistic and continuum mechanical surrogate models, including in the attractive regime, but this suddenly changes if the wall is moved further: in figure 12, we see the carbon nanotube begin to buckle. This buckling cannot be captured by our current finite element model. This phenomenon is also accompanied by large deformations of the nanotube's cross section, which are not accounted for in the current formulation of the continuous beam. These structural changes in the cross section likely explain the apparent softening of the nanotube. Thus the atomistic modeling can be used to detect the range of applicability of the continuum model for a given system. Finally, in figure 13, we show the plot of the eccentricity of the CNT, which is also captured quite well.

5 Conclusion and Outlook

We have demonstrated how the procedure summarized in figure 1 can be used to obtain a surrogate model for atomistic beam structures. To this end, the theory of geometrically exact beams [9] was chosen as a candidate for the description of the substituting continuum mechanical system. To assess the suitability of the

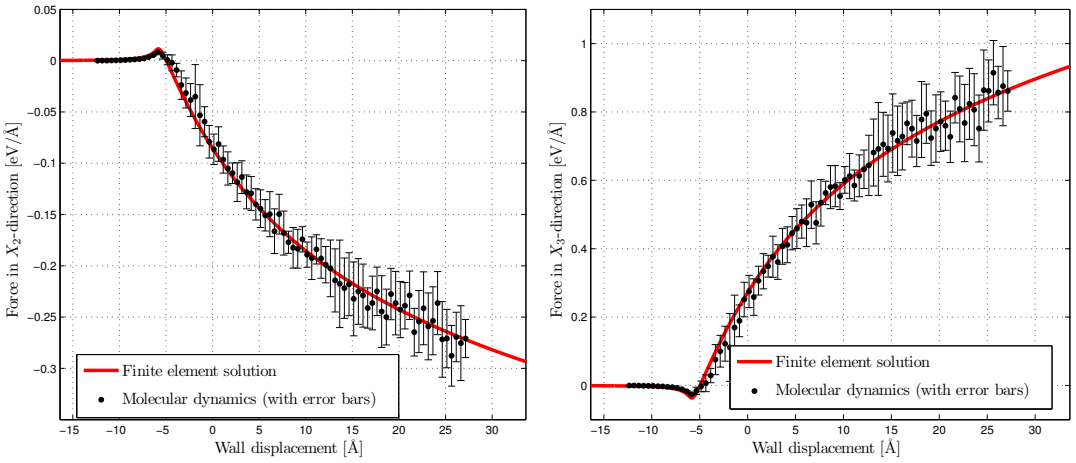

(a) (b)

Figure 11: Carbon nanotube ($n = m = 15$, $L = 381.9\,\text{Å}$): Forces exerted on the beam structure by a moving Lennard-Jones wall. Error bars indicate the standard deviation.

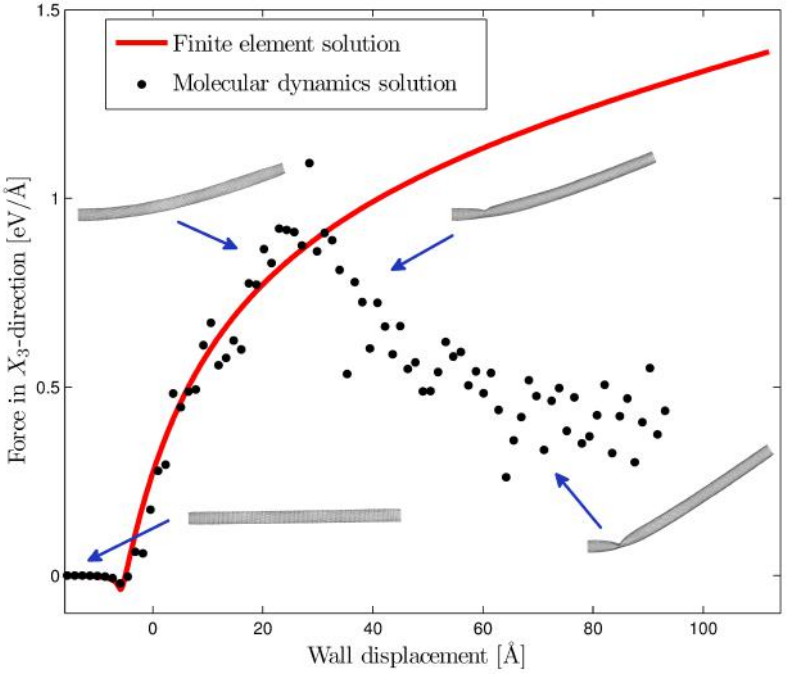

Figure 12: Carbon nanotube ($n = m = 15$, $L = 381.9\,\text{Å}$): Buckling occurs for large displacements of the wall. Exemplary stages of the deformation are also shown.

$n = m$	L [Å]	M_0 [Å^{-1} u]	M_2^{11} [Å u]	M_2^{22} [Å u]
10	383	180	5000	4930
15	382	269	21 900	16 700
20	383	359	39 600	39 000
25	493	449	77 000	76 200

Table 4: Carbon nanotubes: The identified effective length L, mass density M_0 and cross section inertia $M_2^{\alpha\alpha}$, for four systems with CNT indices (n, m).

$n = m$	GA_1 [Å^{2}bar]	GA_2 [Å^{2}bar]	EA [Å^{2}bar]	EI_1 [Å^{4}bar]	EI_2 [Å^{4}bar]	GJ [Å^{4}bar]
10	4.79×10^8	4.76×10^8	1.45×10^9	4.86×10^{10}	4.92×10^{10}	4.70×10^{10}
15	7.09×10^8	7.33×10^8	2.41×10^9	1.66×10^{11}	1.67×10^{11}	1.56×10^{11}
20	8.88×10^8	8.86×10^8	3.12×10^9	3.67×10^{11}	3.75×10^{11}	3.45×10^{11}
25	1.08×10^9	1.10×10^9	4.12×10^9	6.92×10^{11}	6.99×10^{11}	6.93×10^{11}

Table 5: Carbon nanotubes: The identified material parameters for the constitutive law (58), for four systems with CNT indices (n, m).

method, we looked at a Si nanowire and at a CNT, respectively, approaching an infinite, rigid wall. The forces exerted by this wall onto the beam contain uncertainties when determined using MD simulations. The average of these values, however, is matched by the continuum model to a degree that seems acceptable in the considered applications. Geometric agreement was examined based on the eccentricity of the beam and we saw that the main features of the atomistic curves can also be captured well. For larger deflections, however, an increasing systematic discrepancy became apparent. As one of the reasons for the latter, we identified changes in the cross-sectional shape that cannot be captured with the kinematic description of the geometrically exact beam. Hence an obvious future improvement would be to use an extended beam theory, some of which have been mentioned in sec. 3.1. For example, Luongo and Zulli [39] introduce additional strain variables α, β to capture cross-sectional deformations such as warping or ovalization. These

T [K]	GA_1 [Å^{2}bar]	GA_2 [Å^{2}bar]	EA [Å^{2}bar]	EI_1 [Å^{4}bar]	EI_2 [Å^{4}bar]	GJ [Å^{4}bar]
300	8.88×10^8	8.86×10^8	3.12×10^9	3.67×10^{11}	3.75×10^{11}	3.45×10^{11}
450	8.89×10^8	8.86×10^8	2.54×10^9	3.70×10^{11}	3.69×10^{11}	3.22×10^{11}
600	8.65×10^8	8.73×10^8	2.53×10^9	3.60×10^{11}	3.65×10^{11}	3.29×10^{11}
750	8.46×10^8	8.57×10^8	2.50×10^9	3.56×10^{11}	3.35×10^{11}	3.18×10^{11}

Table 6: Carbon nanotubes: The identified material parameters for the constitutive law (58) for systems with $n = m = 15$ and for varying temperature T.

p_d	GA_1 [Å^{2}bar]	GA_2 [Å^{2}bar]	EA [Å^{2}bar]	EI_1 [Å^{4}bar]	EI_2 [Å^{4}bar]	GJ [Å^{4}bar]
0%	7.09×10^8	7.33×10^8	2.41×10^9	1.66×10^{11}	1.67×10^{11}	1.56×10^{11}
1%	6.03×10^8	5.87×10^8	1.82×10^9	1.58×10^{11}	1.59×10^{11}	1.40×10^{11}
2%	5.55×10^8	5.27×10^8	1.76×10^9	1.42×10^{11}	1.44×10^{11}	1.25×10^{11}

Table 7: Carbon nanotubes: The identified material parameters for the constitutive law (58) for systems with $n = m = 15$ and vacancy percentages p_d of removed atoms.

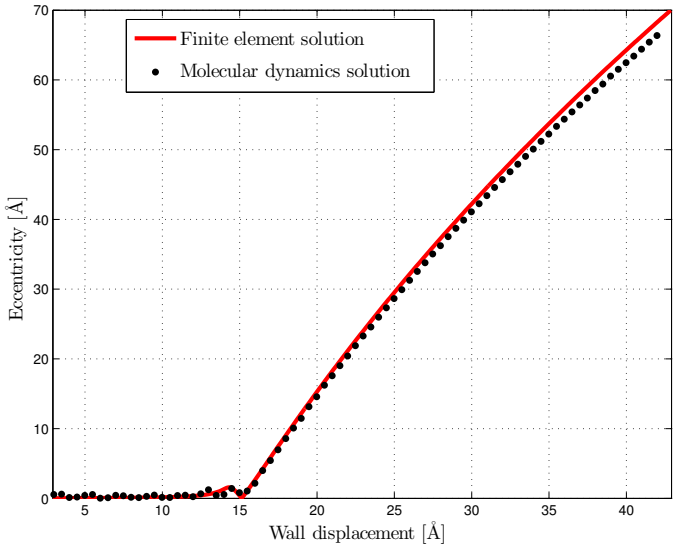

Figure 13: Carbon nanotube ($n = m = 15$, $L = 381.9\,$Å): Eccentricity of the structure at certain wall displacement levels.

satisfy an additional balance equation, typically of the form $B' - D + q = 0$, where q is a distortional force and $D = \partial_\alpha \psi$ and $B = \partial_\beta \psi$ are the new stresses associated with the distortion. To fit the energy density ψ, the general method described in this work would have to be supplemented by appropriate expressions that relate the atomistic degrees of freedom $\boldsymbol{q}, \boldsymbol{p}$ to the macroscopic quantities α, β, D and B based on phase averages.

Another plausible source of the mismatch could be that the linear constitutive law used does not describe the system well over the whole range of deformations. More complex functional forms might therefore be considered [18], or one could adapt an arbitrary three-dimensional constitutive law to the reduced one-dimensional case. In any case, possible rate effects leading to non-relaxed stresses in the VDE at calibration should be avoided by granting sufficiently long equilibration times. The material laws determined in this work could also be applied to adhesion and debonding problems involving thin films [98]. A potential future extension of the present work is posed by coupling the mechanical conservation laws to the general energy balance:

$$\boldsymbol{P} : \dot{\boldsymbol{F}} + \rho_0 r_0 - \operatorname{Div} \boldsymbol{H} = \rho_0 \dot{e}_0, \tag{81}$$

with referential heat source distribution r_0, heat flux vector $\boldsymbol{H}$ and internal energy density e_0. One can then assume, for example, that the latter two quantities depend on instantaneous strain and temperature,

$$\boldsymbol{H} = \boldsymbol{H}(\boldsymbol{\Gamma}, \boldsymbol{\Omega}, T), \quad e_0 = e_0(\boldsymbol{\Gamma}, \boldsymbol{\Omega}, T). \tag{82}$$

In the simplest case, the internal energy is a linear function of temperature: $e_0 = e_0(T) = c_v T + const$, where c_v is the specific heat capacity. It was already shown how the Helmholtz free energy can be determined in a temperature-dependent fashion, $\psi = \psi(\boldsymbol{\Gamma}, \boldsymbol{\Omega}, T)$. However, a new procedure would have to be conceived to obtain suitable continuum mechanical constitutive laws for $\boldsymbol{H}$ and e_0 from atomistic simulations. Numerous studies have attempted to address this problem for three-dimensional bulk systems Fish et al. [27], Admal and Tadmor [28], Lehoucq and Von Lilienfeld [99], Hardy [100], Wagner et al. [101]. One should keep in mind, though, that capturing electron-based heat transfer requires suitable modification of classical MD [102].

On the other hand, the computational costs of the FE simulations are much less compared to the fully atomistic ones. For example, the MD simulation of the beam-wall contact for carbon nanotube ($n = m = 15$) consisting of $N = 8580$ particles takes about 100 h when running on 64 cores in parallel, due to the relatively long simulation time of 98 ns. Compared with this, solving a series of 500 quasi-static continuum problems using 200 finite elements can be done on a conventional

workstation computer in just about one hour, though the one-time calibration phase is not included in this.

We would thus expect large savings in computation time for more complex systems. Some interesting candidates for the near future could for example include multi-walled carbon nanotubes (MWCNT) or larger organic materials like bundles of cellulose strands.

Acknowledgements

The authors are grateful to the German Research Foundation (DFG) for supporting this research under projects GSC 111 and SA1822/5-1.

A Appendix: Analytical expressions for homogeneously deformed beams

To evaluate the integral expression in (27),

$$\mathbf{r}(S) = \mathbf{r}_{\text{in}} + \boldsymbol{\Lambda}_{\text{in}} \left[\int_{s=0}^{S} \exp\bigl(s \cdot \widehat{\boldsymbol{\Omega}}_0\bigr)\, ds \right] \cdot (\boldsymbol{\Gamma}_0 + \boldsymbol{E}_3). \tag{83}$$

we first write $\boldsymbol{\Omega}_0$ in terms of its polar angle θ and azimuth angle ψ:

$$\boldsymbol{\Omega}_0 = \|\boldsymbol{\Omega}_0\| \cdot \begin{bmatrix} \sin\theta\, \cos\psi \\ \sin\theta\, \sin\psi \\ \cos\theta \end{bmatrix}. \tag{84}$$

We then consider the diagonalization $\widehat{\boldsymbol{\Omega}}_0 = \boldsymbol{V} \cdot \boldsymbol{D} \cdot \boldsymbol{V}^*$ with

$$\boldsymbol{D} = \operatorname{diag}\bigl(i\|\boldsymbol{\Omega}_0\|, -i\|\boldsymbol{\Omega}_0\|, 0\bigr), \quad \boldsymbol{V} = \bigl[\boldsymbol{a} + i\boldsymbol{b}, \boldsymbol{a} - i\boldsymbol{b}, \boldsymbol{\Omega}_0/\|\boldsymbol{\Omega}_0\|\bigr], \tag{85}$$

where we introduce

$$\boldsymbol{a} = \frac{1}{\sqrt{2}} \begin{bmatrix} -\cos\theta\, \cos\psi \\ -\cos\theta\, \sin\psi \\ \sin\theta \end{bmatrix}, \quad \boldsymbol{b} = \frac{1}{\sqrt{2}} \begin{bmatrix} -\sin\psi \\ \cos\psi \\ 0 \end{bmatrix}, \tag{86}$$

and $\boldsymbol{V}^*$ is the complex conjugate of $\boldsymbol{V}$. From this we obtain

$$\int_{s=0}^{S} \exp\bigl(s \cdot \widehat{\boldsymbol{\Omega}}_0\bigr)\, ds = \boldsymbol{V} \cdot \left[\int_{s=0}^{S} \exp(s \cdot \boldsymbol{D})\, ds \right] \cdot \boldsymbol{V}^* \tag{87}$$

$$= \boldsymbol{V} \cdot \operatorname{diag}\left(\frac{\exp(iS\|\boldsymbol{\Omega}_0\|) - 1}{i\|\boldsymbol{\Omega}_0\|}, \frac{1 - \exp(iS\|\boldsymbol{\Omega}_0\|)}{i\|\boldsymbol{\Omega}_0\|}, S \right) \cdot \boldsymbol{V}^*, \tag{88}$$

which can be used to obtain the central line $\mathbf{r}(S)$ with respect to basis vectors $\boldsymbol{e}_i$ for any homogeneous strain pair $(\boldsymbol{\Gamma}_0, \boldsymbol{\Omega}_0)$, as is apparent from (83). We are in particular interested in the following resulting configurations for *pure* strains, with $\mathbf{r}_{\text{in}} = \mathbf{0}$, $\boldsymbol{\Lambda}_{\text{in}} = \boldsymbol{I}$ chosen at the beam end $S = 0$.

1. Shear in x-direction, $\boldsymbol{\Gamma}_0 = [\Gamma_1, 0, 0]$, $\boldsymbol{\Omega}_0 = [0, 0, 0]$:

$$\mathbf{r}(S) = \begin{bmatrix} \Gamma_1 \\ 0 \\ 1 \end{bmatrix} \cdot S, \quad \boldsymbol{\Lambda}(S) \equiv \boldsymbol{I} \tag{89}$$

2. Shear in y-direction, $\boldsymbol{\Gamma}_0 = [0, \Gamma_2, 0]$, $\boldsymbol{\Omega}_0 = [0, 0, 0]$:

$$\mathbf{r}(S) = \begin{bmatrix} 0 \\ \Gamma_2 \\ 1 \end{bmatrix} \cdot S, \quad \boldsymbol{\Lambda}(S) \equiv \boldsymbol{I} \tag{90}$$

3. Axial elongation or shortening, $\boldsymbol{\Gamma}_0 = [0, 0, \Gamma_3]$, $\boldsymbol{\Omega}_0 = [0, 0, 0]$:

$$\mathbf{r}(S) = \begin{bmatrix} 0 \\ 0 \\ \Gamma_3 + 1 \end{bmatrix} \cdot S, \quad \boldsymbol{\Lambda}(S) \equiv \boldsymbol{I} \tag{91}$$

4. Bending about x-axis, $\boldsymbol{\Gamma}_0 = [0, 0, 0]$, $\boldsymbol{\Omega}_0 = [\Omega_1, 0, 0]$:

$$\mathbf{r}(S) = \begin{bmatrix} 0 \\ \frac{1}{\Omega_1}(\cos(S \cdot \Omega_1) - 1) \\ \frac{1}{\Omega_1}\sin(S \cdot \Omega_1) \end{bmatrix}, \quad \boldsymbol{\Lambda}(S) = \begin{bmatrix} 1 & 0 & 0 \\ 0 & \cos(S \cdot \Omega_1) & -\sin(S \cdot \Omega_1) \\ 0 & \sin(S \cdot \Omega_1) & \cos(S \cdot \Omega_1) \end{bmatrix} \tag{92}$$

5. Bending about y-axis, $\boldsymbol{\Gamma}_0 = [0, 0, 0]$, $\boldsymbol{\Omega}_0 = [0, \Omega_2, 0]$:

$$\mathbf{r}(S) = \begin{bmatrix} \frac{1}{\Omega_2}(\cos(S \cdot \Omega_2) - 1) \\ 0 \\ \frac{1}{\Omega_2}\sin(S \cdot \Omega_2) \end{bmatrix}, \quad \boldsymbol{\Lambda}(S) = \begin{bmatrix} \cos(S \cdot \Omega_2) & 0 & \sin(S \cdot \Omega_2) \\ 0 & 1 & 0 \\ -\sin(S \cdot \Omega_2) & 0 & \cos(S \cdot \Omega_2) \end{bmatrix} \tag{93}$$

6. Axial torsion, $\boldsymbol{\Gamma}_0 = [0, 0, 0]$, $\boldsymbol{\Omega}_0 = [0, 0, \Omega_3]$:

$$\mathbf{r}(S) = \begin{bmatrix} 0 \\ 0 \\ S \end{bmatrix}, \quad \boldsymbol{\Lambda}(S) = \begin{bmatrix} \cos(S \cdot \Omega_3) & -\sin(S \cdot \Omega_3) & 0 \\ \sin(S \cdot \Omega_3) & \cos(S \cdot \Omega_3) & 0 \\ 0 & 0 & 1 \end{bmatrix} \tag{94}$$

B Appendix: Analytical expressions for Lennard-Jones interactions of a beam

Suppose that for some mapping $f : \mathbb{R}^3 \to \mathbb{R}$ we want to determine the integral

$$\int_{\mathcal{C}} f(\mathbf{r} + \zeta^\alpha \boldsymbol{d}_\alpha)\, d\boldsymbol{\zeta} \tag{95}$$

over the disk $\mathcal{C} = \{\boldsymbol{\zeta} \in \mathbb{R}^2 \mid \|\boldsymbol{\zeta}\| \leq R_{\text{cs}}\}$, for fixed values of $\mathbf{r}$, $\boldsymbol{d}_\alpha$. We can rewrite this as

$$\int_{\mathcal{C}} f\big(\mathbf{r} + \widetilde{\zeta}^\alpha \widetilde{\boldsymbol{d}}_\alpha\big)\, d\widetilde{\boldsymbol{\zeta}}, \quad \widetilde{\boldsymbol{d}}_\alpha := \mathbf{Q}\boldsymbol{d}_\alpha, \tag{96}$$

for any proper orthogonal transformation $\mathbf{Q}$ that leaves $\boldsymbol{d}_3 = \mathbf{Q}\boldsymbol{d}_3$ unchanged. This can be seen by considering the area-preserving transformation

$$T : \mathcal{C} \to \mathcal{C}, \quad \zeta^\alpha = T^\alpha\big(\widetilde{\boldsymbol{\zeta}}\big) = \widetilde{\zeta}^\beta\, \boldsymbol{d}_\alpha \cdot \mathbf{Q}\boldsymbol{d}_\beta. \tag{97}$$

If now f is substituted by $d_E(\cdot)^{-3}$, where $d_E(\boldsymbol{y}) = \boldsymbol{y} \cdot \boldsymbol{\nu} - d$ is the distance to the plane E from sec. 4.1, we can write

$$J_3 := \int_{\mathcal{C}} d_E(\mathbf{r} + \zeta^\alpha \boldsymbol{d}_\alpha)^{-3}\, d\boldsymbol{\zeta} = \int_{\mathcal{C}} d_E\big(\mathbf{r} + \widetilde{\zeta}^\alpha \widetilde{\boldsymbol{d}}_\alpha\big)^{-3}\, d\widetilde{\boldsymbol{\zeta}}. \tag{98}$$

If we choose $\mathbf{Q}$ such that in addition it holds $\widetilde{\boldsymbol{d}}_2 \cdot \boldsymbol{\nu} = \mathbf{Q}\boldsymbol{d}_2 \cdot \boldsymbol{\nu} = 0$ we have

$$d_E\big(\mathbf{r} + \widetilde{\zeta}^\alpha \widetilde{\boldsymbol{d}}_\alpha\big) = \underbrace{\mathbf{r} \cdot \boldsymbol{\nu} - d}_{=:a = d_E(\mathbf{r})} + \widetilde{\zeta}^1\, \underbrace{\mathbf{Q}\boldsymbol{d}_1 \cdot \boldsymbol{\nu}}_{=:b} = a + \widetilde{\zeta}^1 b. \tag{99}$$

Based on this, and introducing $l(t) := \sqrt{R_{\text{cs}}^2 - t^2}$, the integral (98) over $\mathcal{C}$ becomes

$$\int_{\mathcal{C}} \big(a + \widetilde{\zeta}^1 b\big)^{-3}\, d\widetilde{\boldsymbol{\zeta}} = \int_{\widetilde{\zeta}^1 = -R_{\text{cs}}}^{R_{\text{cs}}} \int_{\widetilde{\zeta}^2 = -l(\widetilde{\zeta}^1)}^{l(\widetilde{\zeta}^1)} \big(a + \widetilde{\zeta}^1 b\big)^{-3}\, d\widetilde{\zeta}^1 d\widetilde{\zeta}^2 \tag{100}$$

$$= \int_{\widetilde{\zeta}^1 = -R_{\text{cs}}}^{R_{\text{cs}}} \big(a + \widetilde{\zeta}^1 b\big)^{-3} \cdot 2l\big(\widetilde{\zeta}^1\big)\, d\widetilde{\zeta}^1 \tag{101}$$

$$= \frac{R_{\text{cs}}^2\, \pi}{(a - R_{\text{cs}}\, b)^{\frac{3}{2}} (a + R_{\text{cs}}\, b)^{\frac{3}{2}}} \quad = J_3(a, b, R_{\text{cs}}). \tag{102}$$

In the context of the Lennard-Jones wall interaction, we can note that $d_E\big(\mathbf{r} + \widetilde{\zeta}^\alpha \widetilde{\boldsymbol{d}}_\alpha\big) > 0$ for all $\widetilde{\boldsymbol{\zeta}} \in \mathcal{C}$ since the beam remains in E^+. Hence we have

$$0 < d_E\big(\mathbf{r} + \widetilde{\zeta}^\alpha \widetilde{\boldsymbol{d}}_\alpha\big) = d_E\big(\mathbf{r} + \widetilde{\zeta}^1 \widetilde{\boldsymbol{d}}_1\big) = a + \widetilde{\zeta}^1\, b, \quad \forall \widetilde{\boldsymbol{\zeta}} = \big(\widetilde{\zeta}^1, \widetilde{\zeta}^2\big) \in \mathcal{C}. \tag{103}$$

If we insert the extremal values $\widetilde{\zeta}^1 = \pm R_{\mathrm{cs}}$ this yields the inequalities $a + R_{\mathrm{cs}}\, b > 0$ and $a - R_{\mathrm{cs}}\, b > 0$. This shows that no singularities appear in the denominator of $J_3(a, b, R)$.

One possibility (of two) for a rotation $\boldsymbol{Q}$ that satisfies the aforementioned conditions is given explicitly by

$$\boldsymbol{Q} = \left[\frac{1}{\sin\gamma}(\boldsymbol{d}_3 \times \boldsymbol{\nu}) \times \boldsymbol{d}_3\right] \otimes \boldsymbol{d}^1 + \left[\frac{1}{\sin\gamma}\boldsymbol{d}_3 \times \boldsymbol{\nu}\right] \otimes \boldsymbol{d}^2 + \boldsymbol{d}_3 \otimes \boldsymbol{d}^3, \tag{104}$$

with γ denoting the angle between $\boldsymbol{d}_3$ and $\boldsymbol{\nu}$. It then becomes obvious that $b = \boldsymbol{Q}\boldsymbol{d}_1 \cdot \boldsymbol{\nu} = \sin\gamma$. And as we already know that $a = d_E(\mathbf{r})$ is the distance of the disk center to the wall, we see that

$$J_3 = J_3(a, b, R_{\mathrm{cs}}) = J_3(d_E(\mathbf{r}), \sin\gamma, R_{\mathrm{cs}}) \tag{105}$$

is really just a function of the disk center's distance, the angle between disk and wall normals and the disk radius. Lastly, analogously to J_3, we can also obtain

$$J_9(a, b, R_{\mathrm{cs}}) := \int_{\mathcal{C}} d_E(\mathbf{r} + \zeta^\alpha \boldsymbol{d}_\alpha)^{-9}\, d\boldsymbol{\zeta} = \frac{R_{\mathrm{cs}}^2\,\pi}{64} \cdot \frac{5b^6R_{\mathrm{cs}}^6 + 120a^2b^4R_{\mathrm{cs}}^4 + 240a^4b^2R_{\mathrm{cs}}^2 + 64a^6}{(a - R_{\mathrm{cs}}\, b)^{15/2}(a + R_{\mathrm{cs}}\, b)^{15/2}}. \tag{106}$$

References

[1] Charles M Lieber and Zhong Lin Wang. Functional nanowires. *MRS Bulletin*, 32(02):99–108, 2007.

[2] D. Qian, G. J. Wagner, and W. K. Liu. A multiscale projection method for the analysis of carbon nanotubes. *Comput. Methods Appl. Mech. Engrg.*, 193:1603–1632, 2004.

[3] Rodney S Ruoff, Dong Qian, and Wing Kam Liu. Mechanical properties of carbon nanotubes: theoretical predictions and experimental measurements. *Comptes Rendus Physique*, 4(9):993–1008, 2003.

[4] Brooks D. Rabideau, Animesh Agarwal, and Ahmed E. Ismail. Observed mechanism for the breakup of small bundles of cellulose Iα and Iβ in ionic liquids from molecular dynamics simulations. *The Journal of Physical Chemistry B*, 117(13):3469–3479, 2013. doi: 10.1021/jp310225t. URL `http://pubs.acs.org/doi/abs/10.1021/jp310225t`.

[5] Christian J Cyron and Wolfgang A Wall. Consistent finite-element approach to Brownian polymer dynamics with anisotropic friction. *Physical review. E, Statistical, nonlinear, and soft matter physics*, 82(6 Pt 2):066705–066705, 2010.

[6] Christian J Cyron, Kei W Müller, Andreas R Bausch, and Wolfgang A Wall. Micromechanical simulations of biopolymer networks with finite elements. *Journal of Computational Physics*, 244:236–251, 2013.

[7] I Romero, M Urrecha, and CJ Cyron. A torsion-free non-linear beam model. *International Journal of Non-Linear Mechanics*, 58:1–10, 2014.

[8] M Fixman and J Kovac. Polymer conformational statistics. III. Modified Gaussian models of stiff chains. *The Journal of Chemical Physics*, 58:1564, 1973.

[9] JC Simo. A finite strain beam formulation. The three-dimensional dynamic problem. Part I. *Computer methods in applied mechanics and engineering*, 49(1):55–70, 1984.

[10] Stuart S Antman. *Nonlinear problems of elasticity*, volume 107. Springer, 2005.

[11] Ryan S Elliott, Nicolas Triantafyllidis, and John A Shaw. Stability of crystalline solids — I: Continuum and atomic lattice considerations. *Journal of the Mechanics and Physics of Solids*, 54(1):161–192, 2006.

[12] M Arroyo and T Belytschko. Finite element methods for the non-linear mechanics of crystalline sheets and nanotubes. *International Journal for Numerical Methods in Engineering*, 59(3):419–456, 2004.

[13] Jerry Z Yang and Weinan E. Generalized Cauchy-Born rules for elastic deformation of sheets, plates, and rods: Derivation of continuum models from atomistic models. *Physical Review B*, 74(18):184110, 2006.

[14] Ye Hakobyan, EB Tadmor, and RD James. Objective quasicontinuum approach for rod problems. *Physical Review B*, 86(24):245435, 2012.

[15] Gero Friesecke and Richard D James. A scheme for the passage from atomic to continuum theory for thin films, nanotubes and nanorods. *Journal of the Mechanics and Physics of Solids*, 48(6):1519–1540, 2000.

[16] Bernd Schmidt. On the passage from atomic to continuum theory for thin films. *Archive for rational mechanics and analysis*, 190(1):1–55, 2008.

[17] Karthick Chandraseker, Subrata Mukherjee, Jeffrey T Paci, and George C Schatz. An atomistic-continuum cosserat rod model of carbon nanotubes. *Journal of the Mechanics and Physics of Solids*, 57(6):932–958, 2009.

[18] Chao Fang, Ajeet Kumar, and Subrata Mukherjee. Finite element analysis of single-walled carbon nanotubes based on a rod model including in-plane cross-sectional deformation. *International Journal of Solids and Structures*, 50(1):49–56, 2013.

[19] Youping Chen and James D Lee. Connecting molecular dynamics to micromorphic theory. (I). Instantaneous and averaged mechanical variables. *Physica A: Statistical Mechanics and its Applications*, 322:359–376, 2003.

[20] Youping Chen and James D Lee. Connecting molecular dynamics to micromorphic theory. (II). Balance laws. *Physica A: Statistical Mechanics and its Applications*, 322:377–392, 2003.

[21] Ellad B. Tadmor and Ronald E. Miller. *Modeling Materials: Continuum, Atomistic and Multiscale Techniques*. Cambridge University Press, 2011.

[22] H Jiang, Y Huang, and KC Hwang. A finite-temperature continuum theory based on interatomic potentials. *Journal of engineering materials and technology*, 127(4):408–416, 2005.

[23] SJV Frankland, VM Harik, GM Odegard, DW Brenner, and TS Gates. The stress–strain behavior of polymer–nanotube composites from molecular dynamics simulation. *Composites Science and Technology*, 63(11):1655–1661, 2003.

[24] P. T. Bauman, J. T. Oden, and S. Prudhomme. Adaptive multiscale modeling of polymeric materials: Arlequin coupling and goals algorithms. *Comput. Methods Appl. Mech. Engrg.*, 198:799–818, 2009.

[25] Marcus G Schmidt, Roger A Sauer, and Ahmed E Ismail. Multiscale treatment of mechanical contact problems involving thin polymeric layers. *Modelling and Simulation in Materials Science and Engineering*, 22(4):045012, 2014.

[26] Wen Chen and Jacob Fish. A generalized space–time mathematical homogenization theory for bridging atomistic and continuum scales. *International Journal for Numerical Methods in Engineering*, 67(2):253–271, 2006.

[27] Jacob Fish, Wen Chen, and Renge Li. Generalized mathematical homogenization of atomistic media at finite temperatures in three dimensions. *Computer methods in applied mechanics and engineering*, 196(4):908–922, 2007.

[28] Nikhil Chandra Admal and EB Tadmor. Stress and heat flux for arbitrary multibody potentials: A unified framework. *The Journal of chemical physics*, 134:184106, 2011.

[29] D Davydov and P Steinmann. Reviewing the roots of continuum formulations in molecular systems. part iii: Stresses, couple stresses, heat fluxes. *Mathematics and Mechanics of Solids*, page 1081286513516480, 2013.

[30] DA McQuarrie. *Statistical Mechanics*. University Science, Sausalito, USA, 2000.

[31] Nikhil Chandra Admal and Ellad B Tadmor. A unified interpretation of stress in molecular systems. *Journal of Elasticity*, 100(1-2):63–143, 2010.

[32] Stuart S Antman. The theory of rods. In *Linear Theories of Elasticity and Thermoelasticity*, pages 641–703. Springer, 1973.

[33] I Romero and F Armero. An objective finite element approximation of the kinematics of geometrically exact rods and its use in the formulation of an energy–momentum conserving scheme in dynamics. *International Journal for Numerical Methods in Engineering*, 54(12):1683–1716, 2002.

[34] Juan C Simo and Loc Vu-Quoc. A geometrically-exact rod model incorporating shear and torsion-warping deformation. *International Journal of Solids and Structures*, 27(3):371–393, 1991.

[35] N Silvestre and D Camotim. Nonlinear generalized beam theory for cold-formed steel members. *International Journal of Structural Stability and Dynamics*, 3(04):461–490, 2003.

[36] Marcello Pignataro, Nicola Rizzi, Giuseppe Ruta, and Valerio Varano. The effects of warping constraints on the buckling of thin-walled structures. *Journal of Mechanics of Materials and Structures*, 4(10):1711–1727, 2010.

[37] Ajeet Kumar and Subrata Mukherjee. A geometrically exact rod model including in-plane cross-sectional deformation. *Journal of Applied Mechanics*, 78(1):011010, 2011.

[38] P Lidström. On the equations of motion for curved slender beams using tubular coordinates. *Mathematics and Mechanics of Solids*, page 1081286513487188, 2013.

[39] A Luongo and D Zulli. A non-linear one-dimensional model of cross-deformable tubular beam. *International Journal of Non-Linear Mechanics*, 2014.

[40] JC Simo and Loc Vu-Quoc. A three-dimensional finite-strain rod model. part ii: Computational aspects. *Computer methods in applied mechanics and engineering*, 58(1):79–116, 1986.

[41] Juan Carlos Simo and Loc Vu-Quoc. On the dynamics in space of rods undergoing large motions—a geometrically exact approach. *Computer methods in applied mechanics and engineering*, 66(2):125–161, 1988.

[42] G Jelenić and MA Crisfield. Geometrically exact 3D beam theory: Implementation of a strain-invariant finite element for statics and dynamics. *Computer Methods in Applied Mechanics and Engineering*, 171(1):141–171, 1999.

[43] S Leyendecker, P Betsch, and P Steinmann. Objective energy–momentum conserving integration for the constrained dynamics of geometrically exact beams. *Computer Methods in Applied Mechanics and Engineering*, 195(19): 2313–2333, 2006.

[44] Francois Demoures, Francois Gay-Balmaz, Thomas Leitz, Sigrid Leyendecker, Sina Ober-Blöbaum, and Tudor S Ratiu. Asynchronous variational lie group integration for geometrically exact beam dynamics. *PAMM*, 13(1): 45–46, 2013.

[45] SR Eugster, C Hesch, P Betsch, and Ch Glocker. Director-based beam finite elements relying on the geometrically exact beam theory formulated in skew coordinates. *International Journal for Numerical Methods in Engineering*, 97(2):111–129, 2014.

[46] Ignacio Romero. The interpolation of rotations and its application to finite element models of geometrically exact rods. *Computational mechanics*, 34 (2):121–133, 2004.

[47] FA McRobie and J Lasenby. Simo–Vu Quoc rods using Clifford algebra. *International Journal for Numerical Methods in Engineering*, 45(4):377–398, 1999.

[48] Eva Zupan, Miran Saje, and Dejan Zupan. The quaternion-based three-dimensional beam theory. *Computer methods in applied mechanics and engineering*, 198(49):3944–3956, 2009.

[49] Hongzhi Zhong, Run Zhang, and Naijia Xiao. A quaternion-based weak form quadrature element formulation for spatial geometrically exact beams. *Archive of Applied Mechanics*, pages 1–16, 2014.

[50] E Celledoni and N Säfström. A Hamiltonian and multi-Hamiltonian formulation of a rod model using quaternions. *Computer Methods in Applied Mechanics and Engineering*, 199(45):2813–2819, 2010.

[51] MATLAB. *Version 7.11.0 (R2011a)*. The MathWorks Inc., Natick, Massachusetts, 2011.

[52] M. F. Horstemeyer and M. I. Baskes. Strain tensors at the atomic scale. *MRS Proceedings*, 578, 1 1999. ISSN null. doi: 10.1557/PROC-578-15. URL http://journals.cambridge.org/article_S1946427400297832.

[53] Jonathan A. Zimmerman, Douglas J. Bammann, and Huajian Gao. Deformation gradients for continuum mechanical analysis of atomistic simulations. *International Journal of Solids and Structures*, 46(2):238 – 253, 2009. ISSN 0020-7683. doi: 10.1016/j.ijsolstr.2008.08.036. URL http://www.sciencedirect.com/science/article/pii/S002076830800348X.

[54] Jonathan A Zimmerman, Reese E Jones, and Jeremy A Templeton. A material frame approach for evaluating continuum variables in atomistic simulations. *Journal of Computational Physics*, 229(6):2364–2389, 2010.

[55] John R Ray and Aneesur Rahman. Statistical ensembles and molecular dynamics studies of anisotropic solids. *The Journal of chemical physics*, 80: 4423, 1984.

[56] Steve Plimpton. Fast parallel algorithms for short-range molecular dynamics. *Journal of Computational Physics*, 117(1):1 – 19, 1995. ISSN 0021-9991. doi: 10.1006/jcph.1995.1039. URL http://lammps.sandia.gov.

[57] B. S. Kirk, J. W. Peterson, R. H. Stogner, and G. F. Carey. libMesh: A C++ library for parallel adaptive mesh refinement/coarsening simulations. *Engineering with Computers*, 22(3–4):237–254, 2006.

[58] Roger A. Sauer and Peter Wriggers. Formulation and analysis of a three-dimensional finite element implementation for adhesive contact at the nanoscale. *Computer Methods in Applied Mechanics and Engineering*, 198(49–52):3871 – 3883, 2009. ISSN 0045-7825. doi: 10.1016/j.cma.2009.08.019. URL http://www.sciencedirect.com/science/article/pii/S0045782509002631.

[59] Frank H. Stillinger and Thomas A. Weber. Computer simulation of local order in condensed phases of silicon. *Physical Review B*, 31:5262–5271, 1985.

[60] Jijun Lao, Mehdi Naghdi Tam, Dinesh Pinisetty, and Nikhil Gupta. Molecular dynamics simulation of fcc metallic nanowires: A review. *JOM*, 65(2): 175–184, 2013.

[61] Yong Zhu, Feng Xu, Qingquan Qin, Wayne Y Fung, and Wei Lu. Mechanical properties of vapor–liquid–solid synthesized silicon nanowires. *Nano letters*, 9(11):3934–3939, 2009.

[62] Dai-Ming Tang, Cui-Lan Ren, Ming-Sheng Wang, Xianlong Wei, Naoyuki Kawamoto, Chang Liu, Yoshio Bando, Masanori Mitome, Naoki Fukata, and Dmitri Golberg. Mechanical properties of Si nanowires as revealed by in situ transmission electron microscopy and molecular dynamics simulations. *Nano letters*, 12(4):1898–1904, 2012.

[63] Ronald E Miller and Vijay B Shenoy. Size-dependent elastic properties of nanosized structural elements. *Nanotechnology*, 11(3):139, 2000.

[64] CQ Chen, Y Shi, YS Zhang, J Zhu, and YJ Yan. Size dependence of Young's modulus in ZnO nanowires. *Physical Review Letters*, 96(7):075505, 2006.

[65] Byeongchan Lee and Robert E Rudd. First-principles study of the Young's modulus of Si¡001¿ nanowires. *Physical review B*, 75(4):041305, 2007.

[66] Keonwook Kang and Wei Cai. Size and temperature effects on the fracture mechanisms of silicon nanowires: Molecular dynamics simulations. *International Journal of Plasticity*, 26(9):1387–1401, 2010.

[67] Arif Masud and Raguraman Kannan. A multiscale framework for computational nanomechanics: Application to the modeling of carbon nanotubes. *International journal for numerical methods in engineering*, 78(7):863–882, 2009.

[68] A Krishnan, E Dujardin, TW Ebbesen, PN Yianilos, and MMJ Treacy. Young's modulus of single-walled nanotubes. *Physical Review B*, 58(20): 14013, 1998.

[69] Tobias Hertel, Robert E Walkup, and Phaedon Avouris. Deformation of carbon nanotubes by surface van der Waals forces. *Physical Review B*, 58 (20):13870, 1998.

[70] Jamie H Warner, Neil P Young, Angus I Kirkland, and G Andrew D Briggs. Resolving strain in carbon nanotubes at the atomic level. *Nature materials*, 10(12):958–962, 2011.

[71] Dong Qian, Gregory J Wagner, Wing Kam Liu, Min-Feng Yu, and Rodney S Ruoff. Mechanics of carbon nanotubes. *Applied mechanics reviews*, 55(6): 495–533, 2002.

[72] Sanjay Govindjee and Jerome L Sackman. On the use of continuum mechanics to estimate the properties of nanotubes. *Solid State Communications*, 110 (4):227–230, 1999.

[73] NJ Glassmaker and CY Hui. Elastica solution for a nanotube formed by self-adhesion of a folded thin film. *Journal of applied physics*, 96(6):3429–3434, 2004.

[74] H Üstünel, D Roundy, and TA Arias. Modeling a suspended nanotube oscillator. *Nano letters*, 5(3):523–526, 2005.

[75] Xian-Long Wei, Yang Liu, Qing Chen, Ming-Sheng Wang, and Lian-Mao Peng. The very-low shear modulus of multi-walled carbon nanotubes determined simultaneously with the axial Young's modulus via in situ experiments. *Advanced Functional Materials*, 18(10):1555–1562, 2008.

[76] KM Liew, CH Wong, XQ He, MJ Tan, and SA Meguid. Nanomechanics of single and multiwalled carbon nanotubes. *Physical review B*, 69(11):115429, 2004.

[77] XQ He, S Kitipornchai, and KM Liew. Buckling analysis of multi-walled carbon nanotubes: a continuum model accounting for van der Waals interaction. *Journal of the Mechanics and Physics of Solids*, 53(2):303–326, 2005.

[78] Ning Liu, Yong-Gang Wang, Min Li, and Jiao Jia. Nonlinear buckling analyses of a small-radius carbon nanotube. *Journal of Applied Physics*, 115(15): 154301, 2014.

[79] YY Zhang, CM Wang, WH Duan, Yang Xiang, and Z Zong. Assessment of continuum mechanics models in predicting buckling strains of single-walled carbon nanotubes. *Nanotechnology*, 20(39):395707, 2009.

[80] Tim Gould and David A Burton. A Cosserat rod model with microstructure. *New Journal of Physics*, 8(8):137, 2006.

[81] P Zhang, Y Huang, H Gao, and KC Hwang. Fracture nucleation in single-wall carbon nanotubes under tension: a continuum analysis incorporating interatomic potentials. *Journal of Applied Mechanics*, 69(4):454–458, 2002.

[82] SK Georgantzinos and NK Anifantis. Vibration analysis of multi-walled carbon nanotubes using a spring–mass based finite element model. *Computational Materials Science*, 47(1):168–177, 2009.

[83] Tienchong Chang. A molecular based anisotropic shell model for single-walled carbon nanotubes. *Journal of the Mechanics and Physics of Solids*, 58(9):1422–1433, 2010.

[84] Yu Zhang, Carlo Sansour, Chris Bingham, et al. Single-walled carbon nanotube modelling based on cosserat surface theory. *Recent Advances in Electrical and Computer Engineering*, pages 32–37, 2013.

[85] Sulin Zhang, Steven L Mielke, Roopam Khare, Diego Troya, Rodney S Ruoff, George C Schatz, and Ted Belytschko. Mechanics of defects in carbon nanotubes: atomistic and multiscale simulations. *Physical Review B*, 71(11): 115403, 2005.

[86] Stefan Hollerer. Numerical validation of a concurrent atomistic-continuum multiscale method and its application to the buckling analysis of carbon nanotubes. *Computer Methods in Applied Mechanics and Engineering*, 270: 220–246, 2014.

[87] J. Tersoff. Modeling solid-state chemistry: Interatomic potentials for multicomponent systems. *Phys. Rev. B*, 39:5566–5568, Mar 1989. doi: 10.1103/PhysRevB.39.5566. URL `http://link.aps.org/doi/10.1103/PhysRevB.39.5566`.

[88] LA Girifalco, Miroslav Hodak, and Roland S Lee. Carbon nanotubes, buckyballs, ropes, and a universal graphitic potential. *Physical Review B*, 62(19): 13104, 2000.

[89] R Ansari, F Sadeghi, and S Ajori. Continuum and molecular dynamics study of C_{60} fullerene–carbon nanotube oscillators. *Mechanics Research Communications*, 47:18–23, 2013.

[90] William Humphrey, Andrew Dalke, and Klaus Schulten. VMD: Visual Molecular Dynamics. *Journal of Molecular Graphics*, 14:33–38, 1996.

[91] Marc Robinson and NA Marks. Nanocap: A framework for generating capped carbon nanotubes and fullerenes. *Computer Physics Communications*, 2014.

[92] Ali Ghavamian, Moones Rahmandoust, and Andreas Öchsner. On the determination of the shear modulus of carbon nanotubes. *Composites Part B: Engineering*, 44(1):52–59, 2013.

[93] Jian Ping Lu. Elastic properties of carbon nanotubes and nanoropes. *Physical Review Letters*, 79(7):1297, 1997.

[94] Jean-Paul Salvetat, G Andrew D Briggs, Jean-Marc Bonard, Revathi R Bacsa, Andrzej J Kulik, Thomas Stöckli, Nancy A Burnham, and László Forró. Elastic and shear moduli of single-walled carbon nanotube ropes. *Physical Review Letters*, 82(5):944, 1999.

[95] Michael Griebel and Jan Hamaekers. Molecular dynamics simulations of the elastic moduli of polymer–carbon nanotube composites. *Computer Methods in Applied Mechanics and Engineering*, 193(17):1773–1788, 2004.

[96] Byeong-Woo Jeong, Jang-Keun Lim, and Susan B Sinnott. Elastic torsional responses of carbon nanotube systems. *Journal of applied physics*, 101(8): 084309, 2007.

[97] AR Khoei, E Ban, P Banihashemi, and MJ Abdolhosseini Qomi. Effects of temperature and torsion speed on torsional properties of single-walled carbon nanotubes. *Materials Science and Engineering: C*, 31(2):452–457, 2011.

[98] Roger A Sauer and Janine C Mergel. A geometrically exact finite beam element formulation for thin film adhesion and debonding. *Finite Elements in Analysis and Design*, 86:120–135, 2014.

[99] Richard B Lehoucq and Anatole Von Lilienfeld. Translation of walter noll's "derivation of the fundamental equations of continuum thermodynamics from statistical mechanics". *Journal of Elasticity*, 100(1-2):5–24, 2010.

[100] Robert J Hardy. Formulas for determining local properties in molecular-dynamics simulations: Shock waves. *The Journal of Chemical Physics*, 76 (1):622–628, 1982.

[101] Gregory J Wagner, RE Jones, JA Templeton, and ML Parks. An atomistic-to-continuum coupling method for heat transfer in solids. *Computer Methods in Applied Mechanics and Engineering*, 197(41):3351–3365, 2008.

[102] DM Duffy and AM Rutherford. Including the effects of electronic stopping and electron–ion interactions in radiation damage simulations. *Journal of Physics: Condensed Matter*, 19(1):016207, 2007.